# REPORT DOCUMENTATION PAGE

Form Approved OMB NO. 0704-0188



| 1. REPORT DATE (DD-MM-YYYY) | 2. REPORT TYPE | 3. DATES COVERED (From - To) |
|---|---|---|
| 31-01-2017 | Final Report | 1-May-2013 - 31-Dec-2016 |

**4. TITLE AND SUBTITLE**
Final Report: A New and Comprehensive Approach for the Development of a Compact, High-Performance Rubidium Clock using Raman-Ramsey Interference in Atomic Vapor

**5a. CONTRACT NUMBER**
W911NF-13-1-0152

**5b. GRANT NUMBER**

**5c. PROGRAM ELEMENT NUMBER**
206022

**6. AUTHORS**
Gour S. Pati, Renu Tripathi, S. Shahriar

**5d. PROJECT NUMBER**

**5e. TASK NUMBER**

**5f. WORK UNIT NUMBER**

**7. PERFORMING ORGANIZATION NAMES AND ADDRESSES**
Delaware State University
1200 N. Dupont Highway

Dover, DE 19901 -2277

**8. PERFORMING ORGANIZATION REPORT NUMBER**

**9. SPONSORING/MONITORING AGENCY NAME(S) AND ADDRESS (ES)**
U.S. Army Research Office
P.O. Box 12211
Research Triangle Park, NC 27709-2211

**10. SPONSOR/MONITOR'S ACRONYM(S)**
ARO

**11. SPONSOR/MONITOR'S REPORT NUMBER(S)**
62818-PH-REP.7

**12. DISTRIBUTION AVAILIBILITY STATEMENT**
Approved for Public Release; Distribution Unlimited

**13. SUPPLEMENTARY NOTES**
The views, opinions and/or findings contained in this report are those of the author(s) and should not contrued as an official Department of the Army position, policy or decision, unless so designated by other documentation.

**14. ABSTRACT**
The research was carried out keeping in mind compact, high-performance clock development, which relies on technologies that can be miniaturized. We designed a prototype of the Raman clock using a small (2 cm in length), buffer-gas filled, and isotopically pure 87Rb cell. A fiber-coupled, waveguide electro-optic modulator was used to generate the frequency-modulated CPT beam for the experiments. The experimental setup was operated either by continuous excitation or pulsed excitation for experimentally characterizing CPT and Ramsey interference and testing different optical excitation schemes. Several iterations of the clock physics package were developed in order

**15. SUBJECT TERMS**
Raman Excitation, Ramsey Interference, Coherent Population Trapping, Atomic Clock, Rubidium vapor

| 16. SECURITY CLASSIFICATION OF: | | | 17. LIMITATION OF ABSTRACT | 15. NUMBER OF PAGES | 19a. NAME OF RESPONSIBLE PERSON |
|---|---|---|---|---|---|
| a. REPORT | b. ABSTRACT | c. THIS PAGE | | | Gour Pati |
| UU | UU | UU | UU | | 19b. TELEPHONE NUMBER 302-857-6714 |

## Report Title

Final Report: A New and Comprehensive Approach for the Development of a Compact, High-Performance Rubidium Clock using Raman-Ramsey Interference in Atomic Vapor


## ABSTRACT

The research was carried out keeping in mind compact, high-performance clock development, which relies on technologies that can be miniaturized. We designed a prototype of the Raman clock using a small (2 cm in length), buffer-gas filled, and isotopically pure 87Rb cell. A fiber-coupled, waveguide electro-optic modulator was used to generate the frequency-modulated CPT beam for the experiments. The experimental setup was operated either by continuous excitation or pulsed excitation for experimentally characterizing CPT and Ramsey interference and testing different optical excitation schemes. Several iterations of the clock physics package were developed in order to attain better frequency stability performance of the Raman clock. The experimental work provided the basis to develop a new repeated-query technique for producing Ramsey fringe with high S?N ratio. Atom-field interaction involved in a vapor medium is often more complex. It is difficult to model this interaction in order to predict its influence on CPT characteristics and, hence, the performance of the Raman clock. We developed a comprehensive atomic model to investigate light shift with pulsed excitation. It demonstrated the possibility of reducing (or suppressing) the light shift associated with Ramsey interference for achieving higher frequency stability in the Raman clock.


---

## Enter List of papers submitted or published that acknowledge ARO support from the start of the project to the date of this printing. List the papers, including journal references, in the following categories:

### (a) Papers published in peer-reviewed journals (N/A for none)

| Received | Paper |
|---|---|
| 01/30/2017 | 3 Zachary Warren, S.M. Shahriar, R. Tripathi, G. S. Pati. Experimental and Theoretical Comparison of Different Optical Excitation Schemes for a Compact Coherent Population Trapping Rb Vapor Clock, Metrologia, ( ): . doi: |
| 01/30/2017 | 4 Resham Sarkar, May E. Kim, Renpeng Fang, and Selim M. Shahriar. N-atom collective-state atomic interferometer with ultrahigh Compton frequency and ultrashort de Broglie wavelength, with ? N reduction in fringe width, Physical Review A, ( ): 063629-1. doi: |
| 01/31/2017 | 6 M. S. Shahriar, Ye Wang, Subramanian Krishnamurthy, Y. Tu, G. S. Pati, S. Tseng. Evolution of an N - level system via automated vectorization of the Liouville equations and application to optically controlled polarization rotation, Journal of Modern Optics, ( ): 351. doi: |
| **TOTAL:** | **3** |

**Number of Papers published in peer-reviewed journals:**

## (b) Papers published in non-peer-reviewed journals (N/A for none)

| Received | Paper |
|---|---|

**TOTAL:**

**Number of Papers published in non peer-reviewed journals:**

## (c) Presentations

1. Investigations of AC Stark shift in pulsed Raman-Ramsey interaction for vapor cell clock development
Gour Pati, Z. Warren and S. Shahriar, presented at the SPIE Photonics West, Advances in Slow and Fast Light VII, Feb. 5, 2014, San Francisco, CA.

2. Measurements and characterization of a Rb-based Raman-Ramsey vapor cell atomic clock
Gour Pati, Z. Warren, Renu Tripathi and S. Shahriar, presented at the SPIE Photonics West, Slow Light, Fast Light and Opto-Atomic Precision Metrology - VIII, February, 2015, San Francisco, CA.

3. AC Stark shift in Raman-Ramsey interference using a multi-level system calculation
Gour Pati, Z. Warren and S. Shahriar, presented at the SPIE Photonics West, Slow Light, Fast Light and Opto-Atomic Precision Metrology - VIII, February, 2015, San Francisco, CA.

4. Two-photon resonant Ramsey interference using a repeated-query scheme for atomic clock development
Z. Warren, R. Tripathi and G. Pati, presented at APS Mid-Atlantic Meeting 2016 organized at University of Delaware campus on Oct.15, 2016.

**Number of Presentations:** 4.00

## Non Peer-Reviewed Conference Proceeding publications (other than abstracts):

| Received | Paper |
|---|---|

**TOTAL:**

**Number of Non Peer-Reviewed Conference Proceeding publications (other than abstracts):**

## Peer-Reviewed Conference Proceeding publications (other than abstracts):

Received Paper

**TOTAL:**

**Number of Peer-Reviewed Conference Proceeding publications (other than abstracts):**

## (d) Manuscripts

Received Paper

**TOTAL:**

**Number of Manuscripts:**

## Books

Received Book

**TOTAL:**

Received Book Chapter

**TOTAL:**

## Patents Submitted

## Patents Awarded

## Awards

1. The PI attended SPIE Photonics West meeting, Feb. 2014 in San Francisco and served on the Program Committee for the session on 'Advances in Slow and Fast Light – VII'. The PI also gave the invited talk titled 'Investigations of AC Stark shift in pulsed Raman-Ramsey interaction for vapor cell clock development' at the conference.

2. The PI served as a member of the 'Program Committee' in the session on 'Slow Light, Fast Light and Opto-Atomic Metrology-VIII' organized by SPIE Photonics West Meeting in Feb. 2015, San Francisco, CA. The PI gave an invited talk titled 'AC Stark shift in Raman-Ramsey interference using a multi-level system calculation' at the conference.

3. Co-I, Dr. Renu Tripathi received the DURIP award from Army Research Office (ARO) for the development of a long range, high resolution laser detection and ranging (LADAR) system.
Project Title: Instrument Development for a Long-Range, High-Resolution 3D Imaging Photon Counting LADAR
PI: Renu Tripathi
Funding Agency: DOD DURIP
Award Amount: $191,079.80
Duration: July 15, 2015-Jan 15, 2017.

4. PI served as a member of the 'Program Committee' in the session on 'Slow Light, Fast Light and Opto-Atomic Metrology-X' organized by SPIE Photonics West Annual Meeting in Feb. 2016, San Francisco, CA.

5. The PI served as the 'Lead of the Organizing Committee' in organizing the Delaware Optics Symposium on October 8-9, 2015 at DSU campus. The PI invited several renowned researchers to the DSU campus to deliver invited talks on emerging topics in Optics and Photonics during this symposium, and helped in organizing technical sessions, poster sessions, and an industry exhibit.

6. Awarded the O*STAR Center – Optics for Space Technology & Applied Research Center at DSU under the NASA MIRO 2015 program (center award, Award No. NNH14ZHA001N-MIRO, Period Covered: 09-15 - 08-20). The Co-I, Dr. Renu Tripathi is leading a subproject in O*STAR Center on the Development of sodium LADAR.

7. Graduate student, Mr. Zachary Warren defended the Ph.D. thesis titled 'Coherent Population Trapping and Optical Ramsey Interference for Compact Rubidium Clock Development' on Dec. 6, 2016.

## Graduate Students

| NAME | PERCENT_SUPPORTED |
|---|---|

**FTE Equivalent:**
**Total Number:**

## Names of Post Doctorates

| NAME | PERCENT_SUPPORTED |
|---|---|

**FTE Equivalent:**
**Total Number:**

## Names of Faculty Supported

| NAME | PERCENT_SUPPORTED |
|---|---|

**FTE Equivalent:**
**Total Number:**

## Names of Under Graduate students supported

| NAME | PERCENT_SUPPORTED |
|---|---|

**FTE Equivalent:**
**Total Number:**

## Student Metrics

This section only applies to graduating undergraduates supported by this agreement in this reporting period

The number of undergraduates funded by this agreement who graduated during this period: ..... 2.00
The number of undergraduates funded by this agreement who graduated during this period with a degree in science, mathematics, engineering, or technology fields:..... 0.00
The number of undergraduates funded by your agreement who graduated during this period and will continue to pursue a graduate or Ph.D. degree in science, mathematics, engineering, or technology fields:..... 0.00
Number of graduating undergraduates who achieved a 3.5 GPA to 4.0 (4.0 max scale):..... 0.00
Number of graduating undergraduates funded by a DoD funded Center of Excellence grant for Education, Research and Engineering:..... 0.00
The number of undergraduates funded by your agreement who graduated during this period and intend to work for the Department of Defense ..... 0.00
The number of undergraduates funded by your agreement who graduated during this period and will receive scholarships or fellowships for further studies in science, mathematics, engineering or technology fields: ..... 0.00

## Names of Personnel receiving masters degrees

| NAME |
|---|

**Total Number:**

## Names of personnel receiving PHDs

NAME

**Total Number:**

## Names of other research staff

NAME PERCENT_SUPPORTED

**FTE Equivalent:**
**Total Number:**

## Sub Contractors (DD882)

## Inventions (DD882)

## Scientific Progress

## Technology Transfer

# Final Report

**(May 01, 2013 – December 31, 2016)**

# Table of Content

## 5. Objective

Proposed to investigate pulsed coherent population trapping (PCPT) and Raman-Ramsey (RR) interference in rubidium vapor as a competitive scheme for developing a compact, high performance vapor cell atomic clock for DoD applications.

## 6. Accomplishments

### Year-1

1. Equipment such as single-frequency tunable (rubidium D2, 780 nm to D1, 795 nm wavelength) diode laser (DLC pro, *Toptica Photonics*), phase noise and Allan deviation measurement test-probe (3120A, *Symmetricom*), microwave frequency synthesizer (MG3692C, *Anritsu*), dual-phase DSP lock-in-amplifier (SR830, *Stanford Research Systems*), fiber-pigtailed low-V$\pi$ electro-optic modulator (AZ-0S5-10-PFA-PFA-795, *EOSpace*), rubidium vapor cells (*Triad Technology*), DAQ and digitizer board (USB-6251, PCI-5152, *National Instruments*), RF spectrum analyzer (HP 8562E, *National Test Equipment*), and frequency control electronics (microwave VCXO, PLL, multipliers, and DDS etc.) were purchased for experiments.

2. An experimental system was developed in PI's laboratory using $^{85}$Rb vapor cell to perform complete physical characterization and optimization of RR interference phenomena in rubidium vapor. Results were discussed in the annual report.

3. A compact scheme for generating Raman frequencies using an offset phase-locking scheme was developed in collaboration with Northwestern University (NU).

4. Theoretical investigations were carried out to investigate light shift in RR interference. Light shift was calculated for the single-velocity case and extended to velocity-averaged Doppler-broadened medium. Results obtained from these studies were published in a peer-reviewed journal.

### Year-2

1. CPT and RR interference experiments were extensively performed using a pure isotope $^{87}$Rb vapor cell. Raman beams were generated using a high-bandwidth electro-optic modulator (EOM) in experiments. Problems associated with EOM bias drift was resolved by active temperature control and bias voltage control of EOM.

2. CPT resonance characteristics corresponding to clock transition were investigated using different polarization schemes. Magnetic field dependence of CPT resonance with $lin \parallel lin$ polarization scheme and CPT contrast improvement with other schemes were explicitly studied.

3. Short-term and long-term frequency stability performances of the CPT clock were measured by Allan deviation (ADEV) measurements. CPT clock stability close to $10^{-11}$ at 100 sec was observed.

4. Light-shift associated with RR interference was calculated using a comprehensive sixteen-level atomic model, representing all energy levels and Raman excitations in $^{87}$Rb atoms. The results were compared with the three-level model. The sixteen-level atomic model was used to study CPT resonance characteristics with different polarization schemes.

**Year-3**

1. A compact vapor cell physics package was developed using a small (2 cm long) rubidium (pure $^{87}$Rb isotope) cell. The cell heating and magnetic field designs were optimized for achieving high clock stability. CPT experiments were performed with the compact physics package to determine best condition for achieving high clock stability.

2. Detailed numerical calculations were carried out using the sixteen-level atomic model to determine CPT characteristics with $lin \,||\, lin$, $(\sigma, \sigma)$ and $lin \perp lin$ polarization schemes. Effect of transverse magnetic field is studied on $(\sigma, \sigma)$ polarization to show generation of new Zeeman CPT resonances. Equivalence between $lin \perp lin$ and push-pull optical pumping (PPOP) excitation was established.

3. A low phase-noise electronic phase-locked loop (PLL) was developed for synthesizing rubidium clock frequency. Frequency stabilities of the optimized CPT clock were measured. A higher short-term stability ($\sigma_y \simeq 2.7 \times 10^{-11}$) was measured. Long-term stability close to $\sigma_y \simeq 9 \times 10^{-12}$ for $\tau \simeq 150$ sec was also observed.

4. Design and performance estimation of a miniaturized CPT clock was performed in collaboration with NU. The design showed total power consumption - less than 250 mW, and a compact clock volume of less than 40 cm$^3$.

5. New concept for Heisenberg-limited collective state RR atomic clock was proposed and investigated at NU. This reduces the width of RR fringes by a factor N, and improves the sensitivity of the clock by a factor √N, where N is the number of atoms interrogated in a given time window.

**Year-4 (No-cost extension)**

1. The small cell physics package design is revised to achieve better temperature control of the cell and reduce magnetic field gradient in the cell environment.

2. Demonstrated a new repeated query technique (RQT) as a competitive scheme for generating single resonance Ramsey fringe with high $S/N$ ratio and narrow fringe-width. Ramsey clock experiments are performed using RQT and the conventional single query

technique (SQT). A manuscript is written on this study which will be submitted to the journal for publication.

3. Preliminary characterization of vertical cavity surface emitting laser (VCSEL) for Raman frequency generation has been performed.

## 7. Technical Summary (Year 1-3)

## A. Experiments

### A1. CPT and RR Interference in $^{85}$Rb Vapor

Fig. 1a shows the initial experimental system developed for investigating CPT and RR interference phenomena in $^{85}$Rb vapor. A detailed description of the system was presented in the year-1 report. Raman beam (with frequency difference, $\Delta\nu$ = 3.0356 GHz matching the ground-state hyperfine frequency separation in $^{85}$Rb atoms) in this experimental system, were generated by using an acousto-optic modulator (AOM) in a double-pass configuration. The two Raman

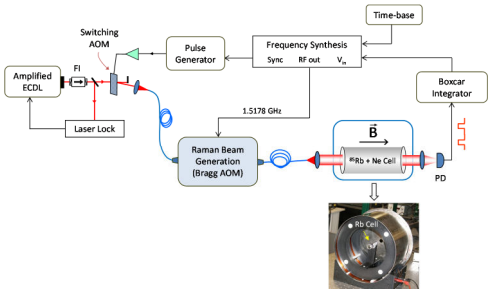


(a)

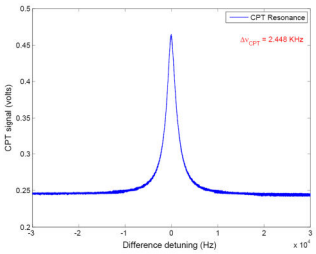


(b)

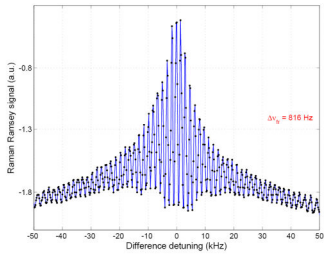


(c)

Fig. 1 (a) Diagram of the experimental system developed for investigating CPT and RR interference phenomena in $^{85}$Rb vapor, and experimentally observed (b) CPT resonance (linewidth ≃ 2.448 kHz), and (b) RR fringes (fringe-width ≃ 816 Hz).

beams were combined in free-space and linearly and orthogonally polarized. They produced Raman excitations in $^{85}$Rb atoms in D1 transitions ($\lambda \simeq 795$ nm) corresponding to hyperfine energy levels $5S_{1/2}$ and $5P_{1/2}$ for observe CPT and RR interference effects. Figs. 1(b,c) show typical CPT resonance and RR fringe observed using this experimental system. Fig. 1b shows CPT resonance with narrow linewidth close to 2.4 KHz for 200 μW total optical power in the Raman beams. In case of RR interference, pulsed CPT excitations were used by generating a long CPT pulse ($\tau_1$ = 200 μs), a free-evolution time, T ≃ 600 μs and a short query pulse ($\tau_2$ = 200 ns). Fig. 1c shows RR fringes with narrow fringe-width close to 816 Hz observed by using

same optical power as in the CPT experiment. The fringes were observed with much higher contrast than the CPT resonance. The experimental system shown in fig. 1a was also operated as a clock to measure its frequency stability. Results indicated that the performance of the locked oscillator was severely degraded by various limiting factors. Order magnitude improvement in frequency stability was expected to be achieved using pure isotope $^{87}$Rb atoms.

## A2. Offset-Phase-Locking of DBR Lasers

In year-1, an offset-phase-locking (OPL) system was developed and tested for Raman beam generation using two compact distributed-Bragg-reflector (DBR) lasers. Fig. 2a shows the picture of a breadboard-mounted OPL system. The OPL system was initially realized using standard PCB current controllers for the DBR lasers. After close scrutiny, it was found that the spectrum of the beat frequency between the two lasers observed at the output of OPL was not narrow enough to produce narrow linewidth CPT resonance in experiments. The current controllers were replaced by faster (high bandwidth) Libbrecht-Hall designs, which eventually produced much narrower OPL spectrum. The performance of the modified OPL system was tested

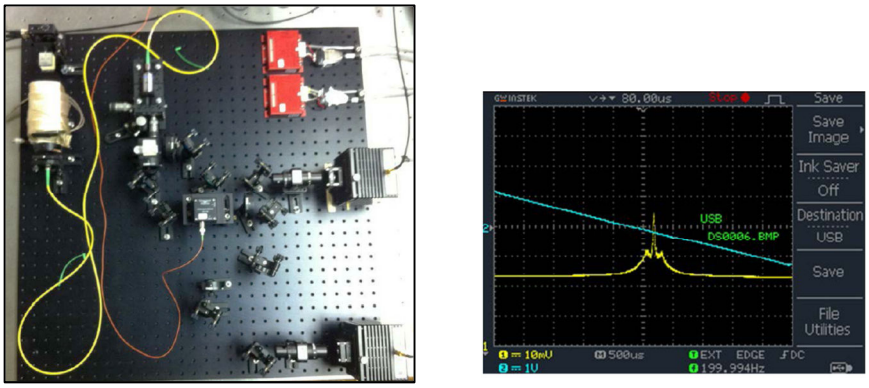


(a) (b)

Fig. 2 (a) Picture of a portable, breadboard-mounted OPL system developed at NU, and (b) CPT resonance observed using the OPL system.

by conducting CPT experiments. Fig. 2b shows the oscilloscope trace of CPT resonance observed using the OPL system. The linewidth of the CPT resonance was found to be approximately 220 KHz, which was limited by the linewidth of the reference VCO used in the OPL system. The OPL system allows one to conveniently generate multi-GHz frequency-shifted Raman beams required for developing $^{87}$Rb based atomic clock.

## A3. Experiments using Pure Isotope $^{87}$Rb Vapor Cell

The diagram in fig. 3 shows the experimental system developed for investigating CPT and Ramsey interference in $^{87}$Rb vapor by employing different polarization schemes for the CPT fields. In particular, the system was used as a CPT clock to measure frequency stability for each polarization scheme. A tunable diode laser (DL PRO, Toptica Photonics) with linewidth less than 1 MHz was used as the light source. A small pure-isotope $^{87}$Rb vapor cell (length = 2 cm, diameter = 1 cm), filled with 10 Torr neon buffer gas was used in the study. The laser beam was sent through a fiber-coupled waveguide electro-optic modulator (EOM, EOSpace AZ-0S5-10-PFA-PFA-795, bias $V_\pi = 1.4$ v) driven by an RF oscillator to produce a frequency-modulated

laser beam for CPT experiments. The EOM was driven by approximately 20 dBm RF power to produce optical sidebands around the laser carrier frequency. The difference in frequency between the first two sidebands was matched close to 6.834 GHz (the hyperfine ground-state frequency of $^{87}$Rb), fine-tuned to account for the buffer gas pressure induced frequency shift ($\Delta f_{buf} = 3.022$ kHz) in the cell.

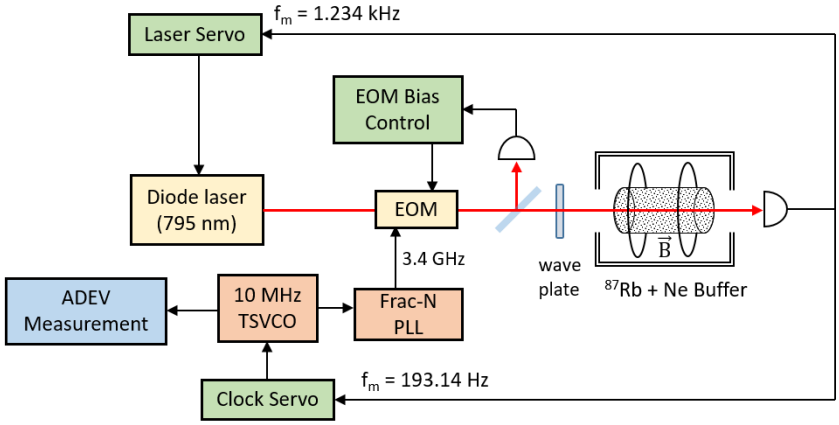


Fig. 3 Experimental system developed for $^{87}$Rb CPT clock. A single photodetector distributes the optical signal and produces independent control signals for the laser servo and the clock servo. The waveplate is either λ/2 or λ/4, for implementing $lin \parallel lin$ or $(\sigma, \sigma)$ polarization schemes.

During experiments, the laser frequency was locked to the Doppler-broadened $^{87}$Rb D1 absorption maximum created by resonant excitation of the modulated laser beam. This enabled us to use a single photodetector for implementing the laser lock as well as the CPT clock. The laser lock is implemented via dither modulation and a laser servo controller shown in fig. 3. The dither modulation frequencies for the laser servo and the clock servo, which operate independently, are chosen to be unequal in order to prevent lock instability caused by interference. The EOM had an undesirable temperature dependence of its bias voltage. Since the bias voltage controls the optical power in the carrier and the sidebands, any temperature drift due to internal heating causes appreciable drift in power in the carrier and the sidebands. The off-resonant carrier also contributed to the CPT background which reduces the contrast in the CPT signal. We actively controlled the EOM bias voltage to minimize the carrier power. This was done by picking off a small fraction of the beam after the EOM, measuring it with a photodiode and implementing an electronic servo by deriving a correction signal from the dithered EOM bias voltage. In addition, an active thermal control of the EOM using a TEC (thermo-electric cooler) and a temperature controller was used to further minimize the drift in the EOM bias voltage. Residual drift in the carrier (or sideband) power was also monitored with a scanning Fabry-Perot etalon (not shown in the figure).

The RF signal at ~3.4 GHz for driving the EOM was synthesized from a 10 MHz temperature-stabilized voltage controlled oscillator (TSVCO, 501-04609A, Wenzel) using a fractional phase-locked loop (Frac-N PLL, LMX2487E, Texas Instruments). The PLL output was internally connected to the on-board 3.417 GHz oscillator via an integrating servo (or loop filter) which allowed us to lock the RF in phase with the master 10 MHz TSVCO. This way, any change to the 10 MHz TSVCO resulted in a proportional change to the RF and hence, the laser modulation frequency. The physics package of the vapor cell comprised a dual layer μ-metal magnetic shield

enclosure surrounding the cell to mitigate residual magnetic fields by approximately 40 dB. We used a pair of Helmholtz coils (diameter = 16.5 cm) mounted inside the enclosure to apply a small uniform axial magnetic field (B ≃ 30 mG) for lifting the Zeeman degeneracies of the $^{87}$Rb atomic states. The rubidium cell was actively temperature controlled ($\Delta T \simeq 100$ mK) with bifilar-twisted resistive nichrome heating wire and a standard K-type thermocouple sensor. The laser beam emerging from the EOM was expanded using a fiber-end collimator to an approximate diameter of 8 mm before passing it through the rubidium cell. A combination of the expanded beam size and frequent collisions of $^{87}$Rb atoms with buffer gas atoms increased the interaction time between the laser fields and $^{87}$Rb atoms for observing narrow linewidth CPT resonance. Sub-kilohertz linewidth CPT resonance, limited by the optical power, was observed by scanning the laser modulation frequency (sweeping the TSVCO) around the two-photon resonant condition. The polarization states for the CPT excitation fields were controlled using a wave plate in the beam path. In the case of $lin \parallel lin$ excitation, a properly oriented half-wave ($\lambda/2$) plate established a particular linear polarization state. To choose $(\sigma, \sigma)$ excitation, the $\lambda/2$ plate was replaced by a quarter-wave ($\lambda/4$) plate. However, to employ $lin \perp lin$ (or PPOP), a polarization-based Michelson interferometer (not shown in fig. 3) was used in the beam path.

## A4. Improved Small Cell Physics Package Design

The ambient environment around the experimental vapor cell significantly determines the clock stability. Factors such as stray magnetic fields, temperature gradients, inhomogeneous applied magnetic field, and buffer induced shift due to cell temperature variation, all contribute to clock frequency errors. Continual improvements to the physics package were made as time and funding allowed, based on the quality of our experimental results. The first small cell physics package that was used is described here followed by a revision for improved heating and magnetic field stability, which was ultimately used in our experiments.

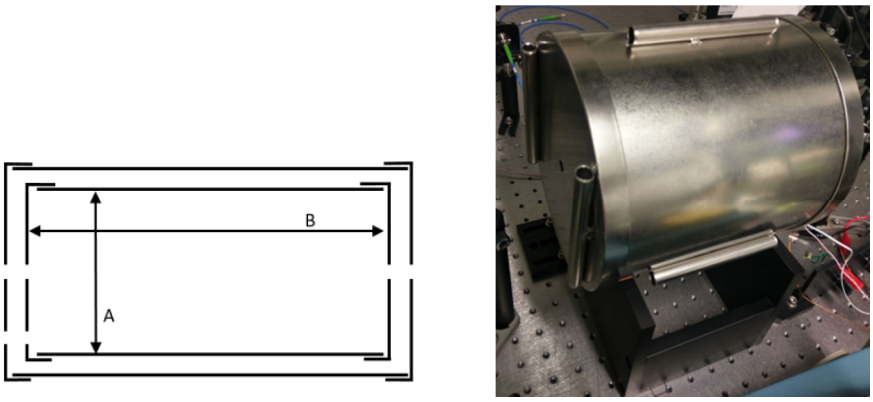


Fig. 4: Schematic and picture of μ-metal chamber on pedestal in the beam path

For small cell studies, we used a pure-isotope $^{87}$Rb vapor cell (optical path = 2.3 cm, diameter = 1 cm), filled with 10 Torr neon buffer gas. The physics package for the vapor cell has an approximate cylindrical volume of 7000 cubic cm. This is composed of a dual layer μ-metal magnetic shield enclosure surrounding the cell for mitigating residual magnetic fields resulting from the Earth and the local environment by approximately 50 dB. The μ-metal magnetic shielding chamber has an internal diameter of 16.5 cm (A) and length of 19 cm (B). There are through-holes for the laser beam on both sets of endcaps and through-holes for wires on one set

of endcaps, shown in fig. 4 schematic. The dual layer shields each have a thickness of 0.16 cm and are separated by 1.27 cm spacers. A plastic pedestal supports the chamber. Figure 4 also shows the chamber *in situ*, and the spacers on the outside allowing it to fit into a third shield, if needed. In this low B-field environment, we used a pair of Helmholtz coils mounted inside the enclosure to apply a small uniform axial magnetic field (B $\simeq$ 30 mG) to lift the Zeeman degeneracy of the $^{87}$Rb atomic states. The Helmholtz coils are lathed from plastic, which have 44 turns of copper wire per coil. The Helmholtz coils have a diameter of ~16.4 cm and are ~1.8 cm wide, with an inner separation of ~8.5 cm.

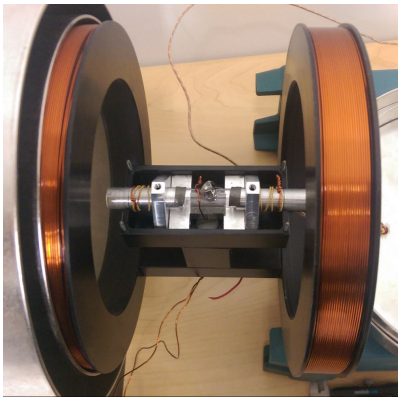

Fig. 5(a) Picture showing Helmholtz coils and small rubidium cell holder.

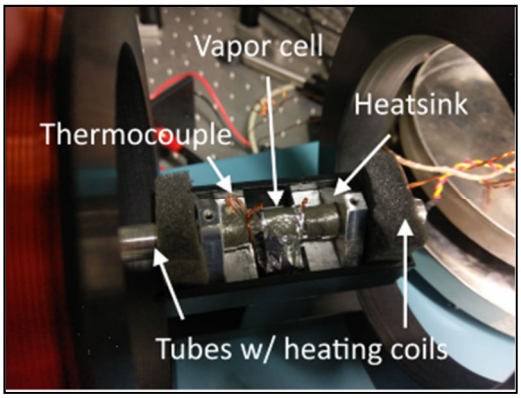


Fig. 5(b) Picture showing rubidium cell in holder between Helmholtz coils with heating wire and thermocouple

Maintaining the separation of the two coils is a horizontal plastic support serving as a base for the plastic pillar which is bolted to a plastic enclosure consisting of a base and a lid which fits on with aluminum pins, shown in fig. 5(a). The enclosure contains the aluminum heatsink which holds the small rubidium cell as shown in the picture in fig. 5(b). The vapor cell must be heated to a sufficiently temperature to produce a high vapor density. Bifilar twisted nichrome wire is wrapped around two aluminum tubes which are set in place to hold the rubidium cell very close to the windows using set screws. This ensures that the primary heat reaches the rubidium cell at the windows, preventing rubidium accumulation on the windows. Double sided thermally conductive tape further secures the rubidium cell and facilitates heat transfer. The glass stem, being furthest away from the heating surfaces, is susceptible to collection of rubidium, risking loss of vapor density, and required further insulation. The cell is covered in aluminum foil and further insulated with a porous foam.

The heating wire is secured to the aluminum tubes with small lengths of copper wire with ends twisted to tighten them into place. Similarly, a K-type thermocouple is bent to touch the glass surface of the vapor cell and held in place with a copper wire, ends twisted until taut. A programmable temperature controller (PTC) (Stanford Research Systems, PTC10) uses PID control to stabilize the temperature by applying varying levels of current to the resistive wires. The vapor cell had active temperature control within $\Delta T \simeq 100$ mK with bifilar-twisted resistive nichrome heating wire and a standard K-type thermocouple sensor. The K-type thermocouple is susceptible to magnetic fields, which could disrupt the homogeneity of the applied magnetic field. One major benefit of this design was that the large bulk of metal reduced the speed of thermal dissipation so that any ambient temperature change was rapidly compensated by the controller. A drawback surfaced, however, when changing the temperature or while optimizing the temperature lock, the response time was very slow – several thermocouple locations were

tried before settling on the position atop the glass cell. During the process of experimentation for improving the temperature stability, we surrounded the plastic enclosure with a phenolic box (fiberglass and resin), but that resulted in preventing the controller from locking to the desired temperature – the response time was severely diminished. To achieve a magnetic field strength of 30 mG, the Helmholtz coils were driven with a current of about 7 mA from a low noise current driver (ILX, LDC3714C).

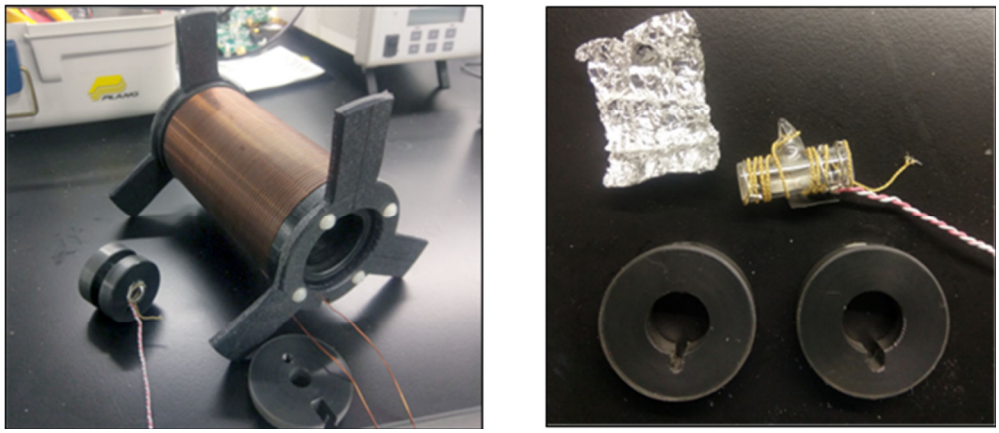

Fig. 6 (left) Solenoid with support fins and mounted vapor cell and (right) Vapor cell wrapped in heating wire alongside aluminum foil insulation and plastic disc cell holders

Upon using the above described physics package, it became evident that we needed to revise the heating and magnetic field designs for the small rubidium vapor cell. For better temperature control and reduction of magnetic field gradient, we made the following modifications. A solenoid with 60 turns of copper wire replaces the Helmholtz coils in the new design, see fig. 6. A spiraled groove cut into the plastic solenoid tube prevents the coiled wire from slipping and helps creating a uniform magnetic field. Three fins on either end of the tube, allowed it to be centered in the μ-metal chamber. The solenoid produces a magnetic field with strength of roughly 40 mG with about 7 mA applied current. To increase the temperature responsivity, the cell is directly wrapped in bifilar twisted nichrome heating wire.

In an attempt to remove the K-type thermocouple, a platinum thin-film temperature sensor (thermistor) was placed in contact with the glass cell. It had a relatively small amount of magnetically-susceptible metal, and was connected to copper leads, to minimize magnetic field disturbance. The cell was wrapped in aluminum foil to retain the applied heat and reduce the amount of current needed to maintain a steady temperature; the components are laid out in fig. 6. A thermistor-based controller (Thorlabs, TC200) was used instead of the previous K-type controller, which was primarily intended for use with vapor cell heating applications. However, this configuration did not provide a stable temperature control and the system was returned to the K-type controller setup. Securing the vapor cell within the solenoid tube required two plastic discs with plastic set-screws. The disc assembly remained stationary in the tube via pressure. Plastic end caps with holes for the laser beam and wires closed off the tube to further reduce the temperature gradient and maintain higher temperature stability. The CPT spectrum obtained with this new physics package showed little to no evidence of magnetic field distortion from the solenoid.

## A5. CPT Results for Different Polarization Schemes

We prepared the modulated laser beam in the $lin \parallel lin$ polarization state, and measured the characteristics of CPT resonance. Fig. 7(left) shows the central CPT resonance observed with $lin \parallel lin$ excitation resonant with the $|F' = 1\rangle$ state for two different axial magnetic field strengths. With low axial magnetic field ($B_z \simeq 30$ mG), a single-peaked CPT resonance with linewidth of 841 Hz and contrast of 7.5% was observed. CPT contrast was measured by calculating $(V_P - V_B)/V_P$ where $V_P$ and $V_B$ are defined as the respective peak and background voltage levels of the CPT signal. The total optical power used in the modulated laser beam was approximately 70 μW. At higher magnetic field ($B_z \simeq 900$ mG), the CPT resonance is split into two separate resonances.

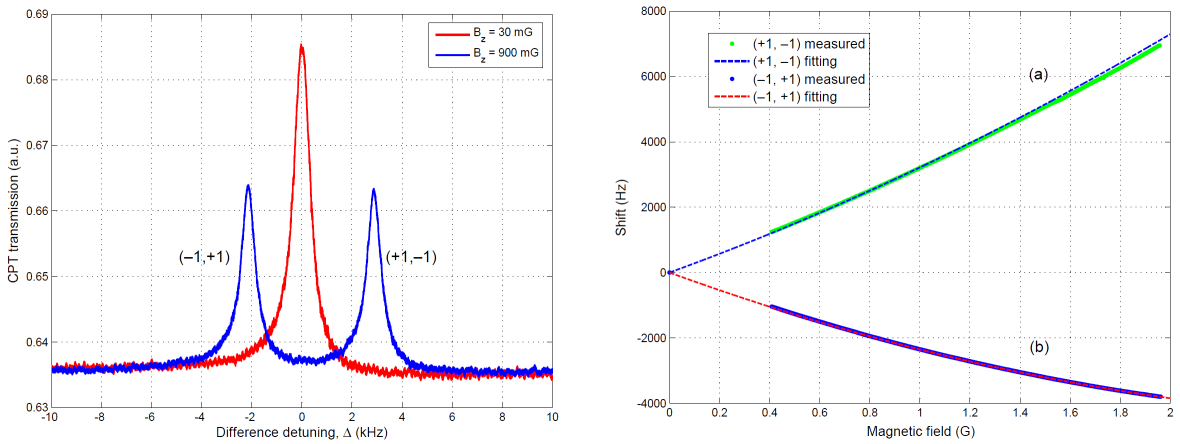


Fig. 7 (left) Magnetic field induced splitting of the central CPT resonance (linewidth = 841 Hz, contrast = 7.5%) generated by $lin \parallel lin$ excitation resonant with $|F' = 1\rangle$ state. Fig. 7 (right) Magnetic field dependencies of (a) the (+1, –1) CPT resonance and (b) the (–1, +1) CPT resonance, shown in left. The dashed lines represent the fittings obtained using the Breit-Rabi equation.

The central CPT resonance consists of two dark states formed by (–1, +1) and (+1, –1) ground state $m_F$ sublevels in $^{87}$Rb. These dark states have higher magnetic field sensitivity than the conventional 0-0 dark state. Fig. 7(right) shows the magnetic field dependencies of (–1, +1) and (+1, –1) CPT resonances produced by the $lin \parallel lin$ scheme. These measurements were obtained by slowly changing the current in the Helmholtz coil while keeping the laser modulation frequency locked to the peak of CPT resonance using an electronic servo, and measuring the shift in the modulation frequency with a frequency counter. Our measurements could only be taken when the (–1, +1) and (+1, –1) resonances were separated by $B_z$ sufficiently enough to allow the servo to lock. The two resonances split asymmetrically as $B_z$ was gradually increased. As expected, the splitting also exhibits a nonlinear dependence on $B_z$. The experimental trends agreed very well with the magnetic field dependencies shown in dashed lines in fig. 7(right) as theoretical fittings obtained from the Breit-Rabi equation:

$$\Delta_{\binom{+1,-1}{-1,+1}} = \omega_{hf} \pm \left(\frac{2g_I\mu_B}{\hbar}\right) B_z + \left(\frac{3}{4}\frac{(g_J - g_I)^2\,\mu_B^2}{2\hbar^2\omega_{hf}}\right) B_z^2 \qquad (1)$$

where $g_I$ is the nuclear spin g-factor and $g_J$ is the electron spin g-factor. We measured the coefficients of linear and quadratic shifts [i.e., the bracketed terms in eqn. (1)], and found them to be in close agreement with published values of 2785.6 Hz/G and 430.94 Hz/G$^2$, respectively.

Traditionally, circular polarization in the form of $(\sigma^+, \sigma^+)$ or $(\sigma^-, \sigma^-)$ has been used in commercial CPT clocks [38–40]. Fig. 8 shows the CPT spectrum produced by $(\sigma^-, \sigma^-)$ excitation resonant with the $|F' = 2\rangle$ state in $^{87}$Rb. The central CPT resonance at $\Delta = 0$ is only formed by the 0-0 dark state. Fig. 8 also shows frequency-shifted Zeeman CPT resonances formed by (–1, –1) and (+1, +1) dark states with frequency shifts proportional to the applied $B_z$ ($\simeq$ 30 mG). The broadening of these Zeeman CPT resonances is attributed to the inhomogeneity of $B_z$ across the cell length. The strengths of Zeeman CPT resonances are indicative of the atomic populations in the (–1, –1) and (+1, +1) dark states. These populations are not equal due to asymmetries in the optical pumping rates into the various Zeeman sublevels.

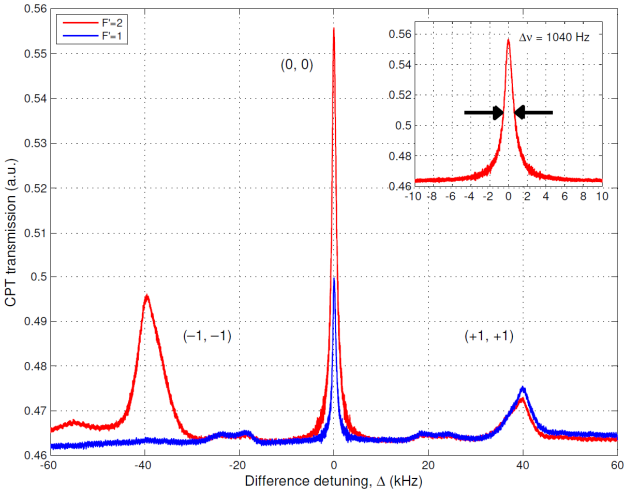


Fig. 8 CPT spectrum produced by $(\sigma^-, \sigma^-)$ excitation resonant with the $|F' = 2\rangle$ state (red) and the $|F' = 1\rangle$ state (blue) for $B_z \simeq 30$ mG. The inset in the figure shows the central CPT resonance produced with linewidth = 1.04 kHz and contrast = 16.7 %.

Although the (-1,-1) Zeeman states are closer to the $|F' = 2, m_F = -2\rangle$ trap state, the (-1,-1) CPT resonance in fig. 8 was found to have a reduced height due to its broadening. Fig. 8 also showed weak transverse Zeeman CPT resonances which are formed midway between (0,0) and (–1, –1) or (+1, +1) resonances due to transverse magnetic fields. The inset in fig. 8 shows the central CPT resonance using a narrow frequency scan (20 kHz) around the two-photon resonance. The linewidth $\Delta\nu$ and contrast C of the central CPT resonance were found to be approximately 1.04 kHz and 16.7%, respectively. We also observed that $(\sigma^-, \sigma^-)$ excitation resonant with the $|F' = 1\rangle$ state produced central CPT resonance with significantly low contrast (C $\simeq$ 4.2%). In addition to the asymmetry in the amplitudes of CPT resonances, it was also seen that Zeeman CPT resonance due to (-1,-1) dark state could not be formed in this case.

Finally, we investigated the $lin \perp lin$ excitation scheme by installing the polarization-based interferometer in our experimental setup. Fig. 9 shows the central CPT resonance (with a Lorentzian fit) produced by $lin \perp lin$ excitation resonant with the $|F' = 1\rangle$ and $|F' = 2\rangle$ states, respectively. For comparing the linewidth and contrast of the CPT resonances, the total optical power used in the laser beam was kept the same ($\simeq$ 70 µW) as that used for the $lin \parallel lin$ and $(\sigma^-, \sigma^-)$ excitations discussed earlier. The measured values of linewidth and contrast for different excitation schemes are summarized in the table below. The central CPT resonance in the $lin \perp lin$ excitation resonant with the $|F' = 2\rangle$ is mainly formed by the 0-0 dark state. We

optimized the path difference between the arms of the interferometer to achieve a maximum contrast of 19% for resonant excitation with the $|F' = 2\rangle$ state. This is nearly 2.4 times higher than that observed for the case where the fields are resonant with the $|F' = 1\rangle$ excitation. However, the observed linewidth for $|F' = 1\rangle$ case was found to be slightly smaller than the $|F' = 2\rangle$ case due to the difference in the strengths of the relevant matrix elements.

**Table 1: Experimentally measured CPT characteristics for different polarization schemes used in resonant excitation with D1 excited states of $^{87}$Rb atoms (N/A – not applicable)**

| Polarization Scheme | Contrast | | Linewidth | | Clock transition |
|---|---|---|---|---|---|
| | $F' = 1$ | $F' = 2$ | $F' = 1$ | $F' = 2$ | |
| $lin \,||\, lin$ | 7.5% | NA | 841 Hz | NA | (–1, +1), (+1, –1) |
| $(\sigma^-, \sigma^-)$ | 4.2% | 16.7% | 780 Hz | 1040 Hz | 0-0 |
| $lin \perp lin$ | 7.8% | 19.0% | 859 Hz | 976 Hz | 0-0 |

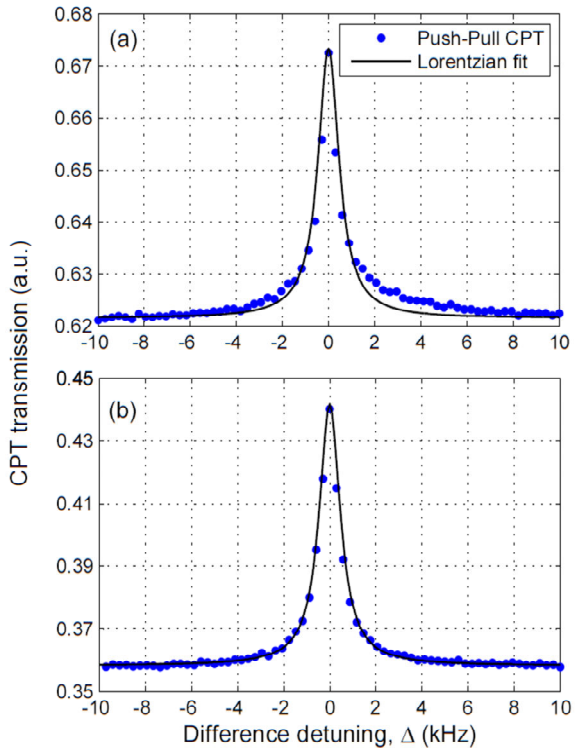


Fig. 9 Central CPT resonance produced by $lin \perp lin$ excitation resonant with (a) $|F' = 1\rangle$ state (linewidth = 859 Hz, contrast = 7.8 %) and (b) $|F' = 2\rangle$ state (linewidth = 976 Hz, contrast = 19%). The solid lines correspond to Lorentzian fits to the CPT profiles.

As can be seen from the summary in table 1, the $lin \perp lin$ excitation is clearly superior to the $lin \,||\, lin$ excitation, especially in terms of the contrast. It also produces a slightly larger contrast than what can be achieved with the $(\sigma, \sigma)$ excitations, although the degree of enhancement in contrast was not very significant. The need to add the interferometer to the cell physics package

may give rise to additional complexity (in terms of volume and weight), thus, making $lin \perp lin$ unsuitable for compact clock designs. However, as mentioned before, a counter-propagating $\sigma^+$ and $\sigma^-$ excitation scheme with similar advantages can be adopted in compact clock design employing cold atoms.

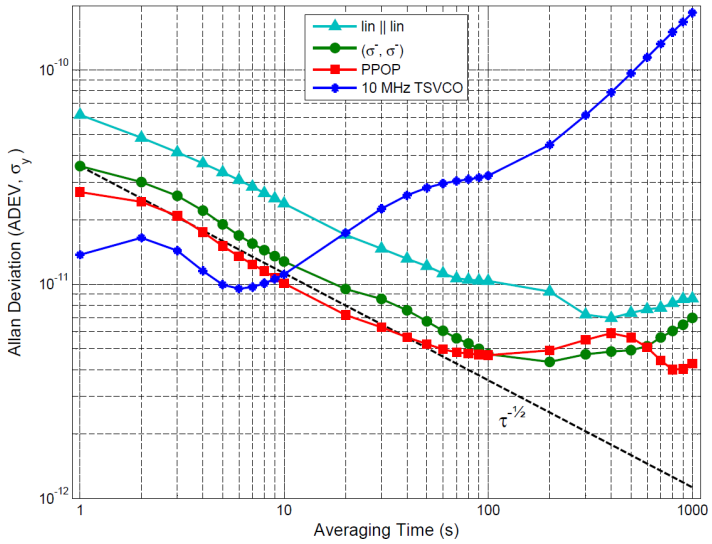


Fig. 10 Frequency stability performance of the rubidium CPT clock measured by ADEV with three: $lin \parallel lin$, $(\sigma^-, \sigma^-)$ and $lin \perp lin$ polarization schemes. Dashed line represents $\sigma_y(\tau) = 3.6 \times 10^{-11}\ \tau^{-1/2}$.

## A6. CPT Clock Frequency stability Measurements

We measured the frequency stability of the rubidium CPT clock prototype by employing all three polarization schemes: $lin \parallel lin$, $(\sigma^-, \sigma^-)$ and $lin \perp lin$. The CPT clock was operated by electronically locking the 10 MHz TSVCO to the peak of the central CPT resonance. The frequency stability (or Allan deviation, ADEV, $\sigma_y$) of the locked oscillator is measured using a phase-noise measurement test probe (Microsemi, 3120A) by referencing it to a rubidium standard (SRS, FS725, $\sigma_y < 2 \times 10^{-11}$ at integration time, $\tau = 1$ sec). Fig. 10 shows a comparison of frequency stabilities for $lin \parallel lin$, $(\sigma^-, \sigma^-)$ and $lin \perp lin$ with the free-running oscillator stability (blue line). The free-running oscillator exhibited a short-term stability, $\sigma_y \simeq 1.4 \times 10^{-11}$ at $\tau = 1$ sec and relatively high instability at longer integration time: for example, $\sigma_y \simeq 1.9 \times 10^{-10}$ at $\tau = 1000$ sec. The CPT locked oscillator showed improved long-term stabilities for all excitations: for example, $\sigma_y \simeq 4.7 \times 10^{-12}$ at $\tau = 100$ sec using $(\sigma^-, \sigma^-)$ excitation. It should be noted that a well-engineered CPT clock should produce close to shot-noise limited stability which is given by

$$\sigma_y(\tau) = \frac{1}{Q}\frac{1}{\mathrm{SNR}}\tau^{-1/2}, \qquad (2)$$

where $Q = \nu_{hf}/\Delta\nu$ represents the quality factor of CPT resonance, and SNR is the signal-to-noise ratio for integration over one second. The dashed line drawn in fig. 10 shows the expected shot-noise limited stability (i.e. $\sigma_y \propto \tau^{-1/2}$) for the $(\sigma^-, \sigma^-)$ excitation with a starting stability $\sigma_y \simeq 3.6 \times 10^{-11}$ at $\tau = 1$ sec. The CPT clocks for all three schemes did not seem to produce shot-noise limited stability for $\tau$ exceeding 100 sec. Frequency stability in the order of $10^{-13}$ has been

reached in rubidium CPT clocks at $\tau$ exceeding 1000 sec . The performance of our CPT clock was limited by various sources of long-term frequency drifts in the system. The major source of frequency drift was related to optical power drift associated with the fiber pigtailed EOM. The power drift was caused by stress and temperature-induced polarization rotation in the fiber, coupled with polarization-dependent modulation properties of the EOM. Other sources of frequency drifts such as cell temperature instability and magnetic field fluctuations were also affecting the long-term stability performance of our CPT clock. Under these circumstances, a comparison of frequency stabilities shown in fig. 10 indicated that $lin \parallel lin$ excitation exhibits the poorest performance of all, both in terms of short-term (due to poor signal contrast) and long-term (possibly due to its high magnetic field sensitivity) stabilities. A long-term stability of $\sigma_y \simeq 9 \times 10^{-12}$ for $\tau \simeq 150$ sec was found in this case. The highest short-term stability ($\sigma_y \simeq 2.7 \times 10^{-11}$) was found in the case of $lin \perp lin$ excitation due to its high CPT contrast. However, the long-term performance of the $lin \perp lin$ CPT clock was affected due to imperfections in the interferometer. Fluctuations in polarization states of the sidebands were caused by vibrations and thermal expansions in the interferometer. Small extinction ratio of the PBS led to polarization leakage in the arms and hence, power drift at the output of the interferometer. These problems can be mitigated by employing a high extinction PBS in a monolithically designed interferometer.

## B. Theoretical Investigations of Light Shift in RR Interference

Light shift properties of CPT are not directly applicable to RR interference because of the pulsed excitation mechanism involved in RR interference. We have investigated RR light shift using the computational model based on the density-matrix equations for a generalized three-level system without invoking the adiabatic approximation.

### B1. Three-Level Atomic Model

We have solved the time-dependent density-matrix equations for pulsed excitation to investigate RR light shift. The following initial conditions were used prior to the CPT pulse: $\rho^0_{ij\ (i\neq j)} = \rho^0_{33} = 0$, $(\rho_{11} + \rho_{22})^0 = 1$, and $(\rho_{11} - \rho_{22})^0 = \rho^0$, where $\rho^0$ is assigned a non-zero value to create unequal initial population between the ground-states. Fig. 11 shows the phase shift measured using $\rho_{33}$ (excited state population) as a function of the average laser frequency detuning, $\delta$. The result is obtained by using different average Rabi frequencies (or intensities) of the CPT pulse, and by considering equal intensities for the Raman beams in the CPT pulse. The following pulse parameters were used: $\tau_c$ = 200 μs, T = 1 ms and $\tau_q$ = 100 ns. An initial ground-state population difference corresponding to $\rho^0 = 0.2$ has been used. The result illustrates reduction in phase/light shift due to pulse saturation (i.e. $\Omega\tau_c \gg 1$) for higher light intensities. The result also shows the comparison between the computational results (solid line) and the analytic results obtained using adiabatic approximation (dashed line). The computational results allowed us to estimate RR light shift more accurately than those obtained using the adiabatic approximation. RR light shift gets adequately suppressed for $\Omega \geq \Gamma/20$ over a range of $\delta$ close to $-\Gamma \leq \delta \leq \Gamma$. Light shift in the unsaturated region is found to oscillate (between positive and negative values), exhibiting nonlinear dependence on $\delta$. The results in fig. 11 also provided information regarding the long-term frequency stability of a Raman clock limited by the

variation in δ, which can be potentially caused by sources such as laser drift, jitter, and linewidth broadening.

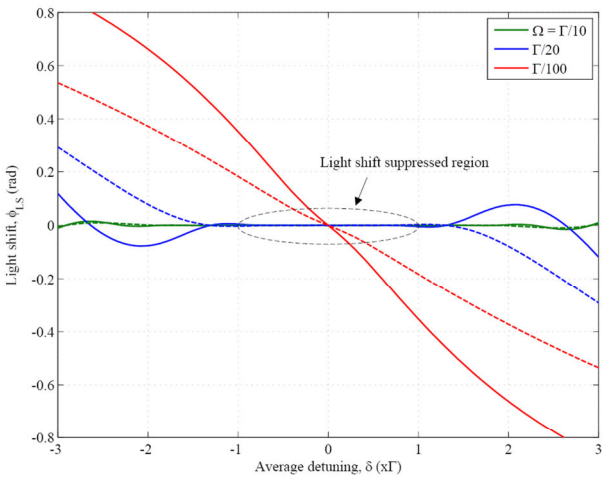


Fig. 11: Light shift, $\boldsymbol{\varphi_{LS}}$ versus δ calculated using $\boldsymbol{\rho_{33}}$. Solid lines represent numerically computed values, and dashed lines show analytical values given in eqn. (4.2). The following parameters were used in the calculations: $\tau_c$ = 200 μs, T = 1 ms, $\tau_q$ = 100 ns, $\boldsymbol{\Omega_1} = \boldsymbol{\Omega_2}$ $(\boldsymbol{\rho_{11} - \rho_{22}})^{\boldsymbol{0}}$ = 0.2 and γ = 0. The encircled region shows the region of light shift suppression.

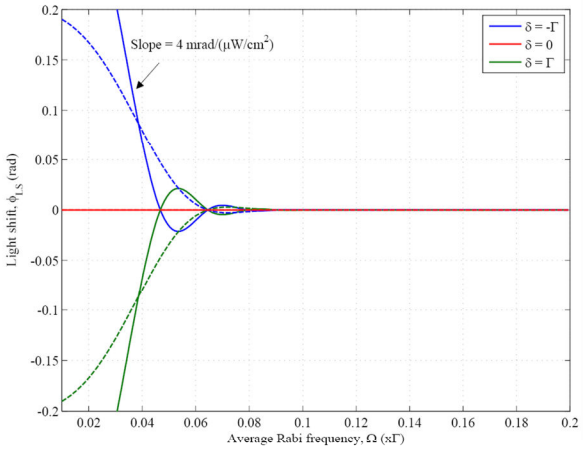


Fig. 12: RR light shift calculated as a function of the average Rabi frequency, Ω, of the CPT pulse. Solid lines show numerical values, and dashed lines show analytical values obtained using eqn. (3). The following parameters were used in the calculations: $\tau_c$ = 100 μs, T = 1 ms, $\boldsymbol{\tau_q}$ = 100 ns, $\boldsymbol{\Omega_1} = \boldsymbol{\Omega_2} = \boldsymbol{\Omega}$, $\boldsymbol{(\rho_{11} - \rho_{22})^0}$ = 0.2 and $\boldsymbol{\gamma}$ = 0. For δ = 0, both numerical and analytical results show zero light shift over the entire range of intensity as expected.

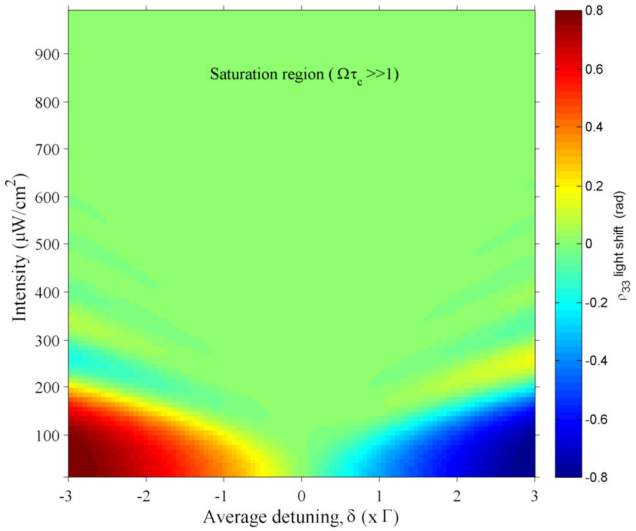


Fig. 13: Color-coded 2D plot showing light shift, $\boldsymbol{\varphi_{LS}}$ as functions of average detuning, δ and intensity, I of the CPT pulse. Saturation intensity ($I_{sat}$ = 3 mW/cm$^2$) for a rubidium atom is considered in converting Ω to an intensity axis. The following parameters were used in the calculations: $\tau_c$ = 100 μs, T = 1 ms, $\boldsymbol{\tau_q}$ = 100 ns, $\boldsymbol{\Omega_1} = \boldsymbol{\Omega_2}$, $\boldsymbol{(\rho_{11} - \rho_{22})^0}$ = 0.2 and $\boldsymbol{\gamma}$ = 0.

Fig. 12 shows the computed RR light shift as a function of Ω of the CPT pulse. RR light shift is close to zero over the whole range of Ω when δ is set equal to zero. For large, non-zero values of δ (e.g. $\delta = \pm\Gamma$), oscillation in light shift with Ω is observed presumably due to weak excitation with the CPT pulse. At higher Ω (or intensity) of the CPT pulse, amplitudes of these oscillations

quickly diminish by virtue of the strong interaction. The result once again shows that RR light shift can be significantly small under strong excitation conditions. Considering mono-velocity atoms and assuming a saturation intensity, $I_{sat}$, of 3 mW/cm$^2$, one can use this result to calculate RR light shift as a function of average intensity, $I \simeq (\Omega/\Gamma)^2 I_{sat}$, of the CPT pulse. One can also estimate the slope of RR light shift in the unsaturated or saturated regions by using this plot. Fig. 13 is a color-coded map generated using the computation to illustrate the properties of RR light shift as a function of both the average detuning, $\delta$, and intensity, I, of the CPT pulse. The uniformly colored region in the plot where the pulse saturation condition ($\Omega\tau_c \gg 1$) is satisfied, corresponds to a small (close to zero) value of RR light shift. The plot also shows oscillations in light shift (as color change) at lower intensities below 500 μW/cm$^2$ and for $4 \leq |\delta| \leq 18$ MHz. The range of ($\delta$ and I) chosen in this map are realistic and can arise in the experiment due to possible laser drift, linewidth broadening, lock instability and/or intensity noise, etc. Therefore, it can be used to get a first-hand estimate of the light shift and long-term frequency stability of the RR clock. For example, the slope of RR light shift can be reduced to an extremely small value below 0.001 Hz mW$^{-1}$ cm$^2$ by using a strong excitation condition.

## B2. Sixteen-Level Atomic Model

The three-level atomic model is only an approximation to the real atom which, in practice, may have laser fields interacting with multiple energy levels. In the case of an atomic clock employing CPT or Ramsey interference, it is necessary to include all the energy levels of $^{87}$Rb atoms in the atomic modeling in order to describe the behavior of the atomic clock accurately. A comprehensive sixteen-level atomic model was created using the Liouville density-matrix equation**,** taking into account all relevant Zeeman sublevels of $^{87}$Rb atoms. Fig. 14 shows the flow diagram with steps involved in finding the steady-state and time-dependent solutions for the sixteen-level atomic model. The steps were implemented using a MATLAB program. The time-dependent solutions were used to calculate RR light shift. Fig. 15 shows the comparison of light shift between the three-level (dashed) and multi-level (solid) models. The results show a small, but important difference between light shift characteristics. The result obtained from three-level model indicates a reduction in phase/light shift due to pulse saturation which occurs for higher Rabi frequencies ($\Omega \geq \Gamma/20$) or higher light intensity of the CPT pulse. In this case, RR light shift is found to be adequately suppressed over a range of $\delta$ close to $-\Gamma \leq \delta \leq \Gamma$. The sixteen-level calculation shows a similar result, but gives a more accurate result for predicting light shift in real atoms. In this case, it is found that higher CPT pulse

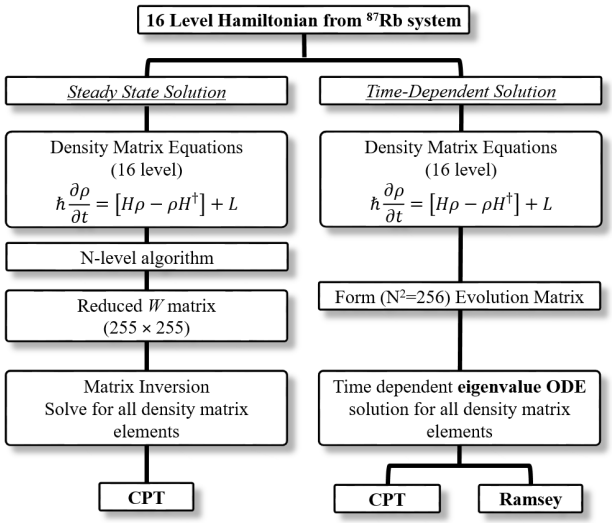


Figure 14: Flow diagram for finding steady state and time-dependent solutions to the density-matrix equations representing a sixteen-level atomic system.

intensity is needed to reach saturation, and suppress the light shift to a small value. Light shift in the unsaturated region oscillates and exhibits a nonlinear dependence on δ.

Fig. 16 shows calculated RR light shift as a function of average Rabi frequency, Ω (or intensity) of the CPT pulse. The result again shows a comparison between three-level model (dashed line) and sixteen-level model (dotted line). In both models, RR light shift is found to be nearly zero over the entire range of Ω when δ is set precisely equal to zero. This agrees with our analytical prediction. For large, nonzero values of δ (e.g. $\delta = \pm\Gamma$), oscillation in light shift with Ω is observed in both models due to weak Raman excitation with the CPT pulse. At higher Ω (or intensity) of the CPT pulse, amplitudes of these oscillations is found to diminish rapidly in case of three-level model by virtue of strong interaction. However, the amplitude of light shift

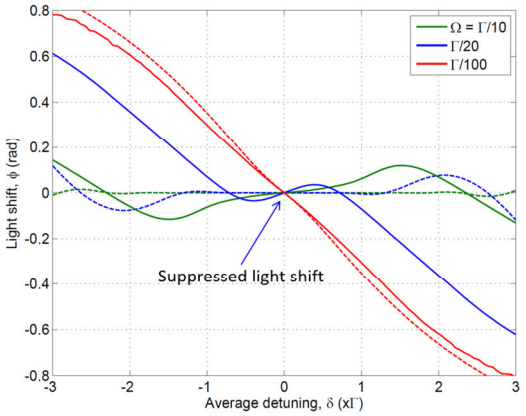


Fig. 15 Light shift, $\boldsymbol{\varphi_{LS}}$ versus δ calculated using $\boldsymbol{\rho_{33}}$. Solid lines represent the numerically computed values from the multi-level model, and dashed lines show the three-level model values. The following parameters were used in the calculations: $\tau_c$ = 200 μs, T = 1 ms, $\tau_q$ = 100 ns, $\boldsymbol{\Omega_1} = \boldsymbol{\Omega_2}$ $(\boldsymbol{\rho_{11} - \rho_{22}})^{\boldsymbol{0}}$ = 0.2 and γ = 0. A shift of 0.5 rad ≡ 80 Hz.

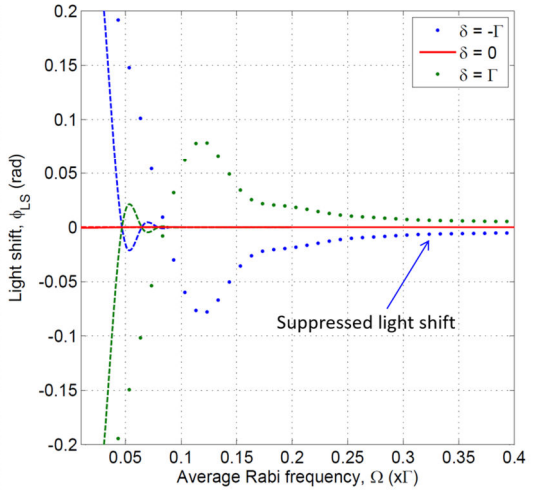


Fig. 16 RR Light shift calculated as a function of average Rabi frequency, **Ω**, of the CPT pulse. Dotted lines represent the numerically computed values from the sixteen-level model, and dashed lines show the three-level model values. The following parameters were used in the calculations: $\tau_c$ = 100 μs, T = 1 ms, $\tau_q$ = 100 ns, $\boldsymbol{\Omega_1} = \boldsymbol{\Omega_2}$ $(\boldsymbol{\rho_{11} - \rho_{22}})^{\boldsymbol{0}}$ = 0.2 and γ = 0.

oscillation is found to be much larger in the sixteen-level case. The period of oscillation is also found to be much longer in this case, possibly due to the presence of multiple off-resonant excitations. However, both models give rise to the same conclusion that RR light shift can be reduced to a small value by using a strong initial CPT pulse. The sixteen-level results, in general, provide more accurate information regarding the long-term frequency stability of the Raman clock, limited by sources such as laser drift, jitter, and linewidth broadening etc.

## C. Miniaturized CPT Atomic Clock Design using Very Low Power

In collaboration with NU, we developed a detailed design of a miniaturized clock that would consume less than 250 mW, with a volume of less than 40 $cm^3$, and carried out a detailed performance analysis to show that it would reach a stability better than $3X10^{-13}/\sqrt{\tau}$ in the long term, where $\tau$ is the interrogation time expressed in seconds.

**Basic Design:** The complete system for our proposed miniature CPT clock is shown schematically in fig. 17. Two different versions of the physics package are shown schematically in fig. 18 and fig. 19, and the Rb cell chamber is shown in fig. 20. We describe briefly these assemblies.

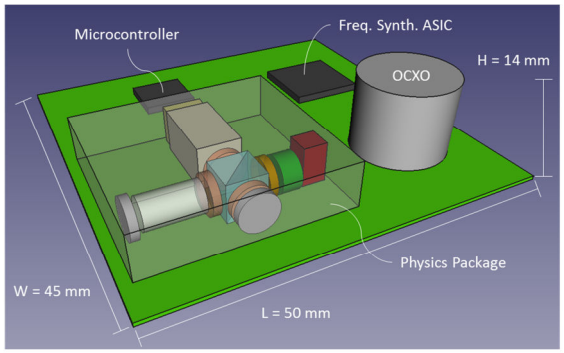


Fig. 17 Schematic, complete, view of the miniature CPT clock system. In this, we have considered using the physics package shown in fig. 18. If the physics package shown in fig. 19 is used, the view would differ accordingly, without affecting the parallelopiped volume.

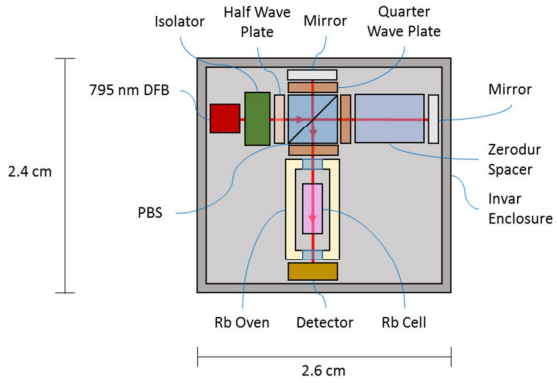


Fig 18 Schematic view of one version of the physics package, containing the vapor cell, the laser, the detector and the interferometer for producing the lin⊥lin polarization.

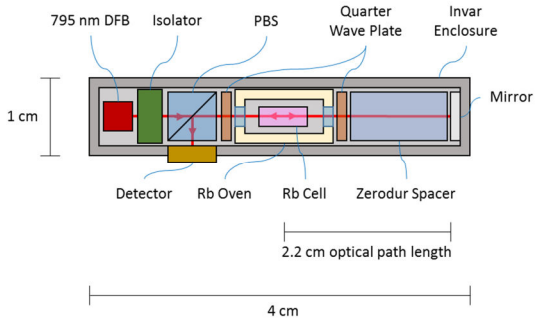


Fig. 19 Schematic view of another possible version of the physics package, containing the vapor cell, the laser, the detector and a reflector, for producing the effective lin⊥lin excitation at the center of the cell.

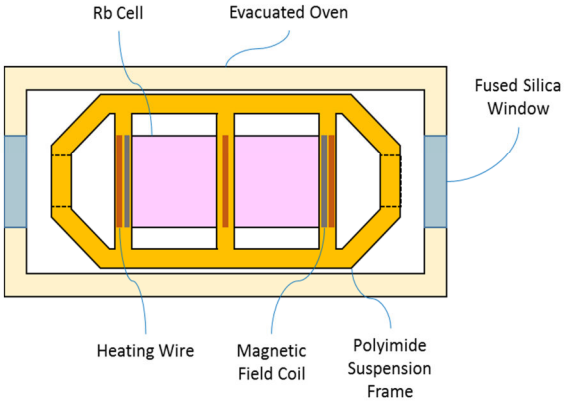


Fig. 20 Schematic view of the Rb vapor cell, suspended with polyimide.

There are two possible configurations for the physics package: One version has a Michelson polarization interferometer (Fig. 18), while the other uses the double-passed configuration (Fig. 19). The Michelson interferometer results in the lin⊥lin polarization for the CPT process. Similarly, the double-pass configuration also produces an effective lin⊥lin configuration, as long as the distance from the mirror to the cell is one quarter of the wavelength corresponding to the frequency difference (6.8 GHz) between the two CPT beams. Both configurations can be constructed using similar techniques and components. The physics package components would be rigidly mounted to an invar plate to preserve alignment, and the entire package would be encapsulated in a mu-metal-lined enclosure to provide magnetic shielding. Electrical connections would be passed through the bottom of the package to allow for attachment to a PCB (Printed Circuit Board). A temperature sensor would also be incorporated into the external housing to allow for software correction of external temperature fluctuations. When assembled, the package with the Michelson interferometer would be 2.4 cm by 2.6 cm by 1.5 cm in size (1 cm for the

main body of the package, with 5 mm of heat sink protruding beyond), for a total parallelopiped volume of 9.36 $cm^3$, while the double-pass configuration package would be 1 cm by 1.5 cm by 4 cm, for a total volume of 6 $cm^3$.

The laser would be the custom, high-speed DFB laser. It would be mounted on a small thermoelectric cooler (TEC) that would maintain it at a constant operating temperature of 90ºC. The back side of the TEC would be coupled to a passive heat sink that would protrude from the physics package to provide a path for heat removal. The DFB would be collimated by a small lens (not shown; placed as close as is practical to the emitting facet) to a beam diameter of ~1 mm, then passed through an ultra-compact Faraday isolator. This isolator would provide >38 dB of isolation at the cost of an insertion loss of ~3.5 dB. The laser would then pass through a polarizing beam cube. Half-wave and quarter wave plates would be affixed at appropriate angles in the optical chain to control the polarization as necessary. In both designs, a Zerodur spacer would be used to increase the effective optical path length (in the longer arm of the Michelson interferometer in one case, between the cell and the retro-reflection mirror in the other).

The rubidium cell itself (2 mm across by 5 mm long), would be filled with rubidium and an appropriate mixture of buffer gases (Argon and Nitrogen), with the relative ratio chosen to ensure that the pressure shifts from the two gases cancel each other at the operating temperature. Its windows will be AR-coated for 795 nm. Magnetic field coils would be mounted (via adhesive or lithography) on the ends of the cell, and bifilar heating coils would be mounted on the ends and in the middle. The cell would be mounted in an evacuated chamber on a polyimide suspension system, as is shown in fig. 20. The suspension system would be fabricated by pattering photosensitive polyimide on silicon, then backside etching to release it. Leads for the magnetic field and heating coils, as well as temperature sensors, would be patterned into the polyimide during fabrication, then attached to the cell leads during mounting. The cell would be attached to the mounts, then the mounts would be, in turn, attached to a spacer with holes in either end to allow passage of the laser. The entire assembly would be mounted on a leadless chip carrier, then it would be enclosed under vacuum by a mu-metal-coated ceramic enclosure set with 2 mm diameter AR-coated windows that would line up with the cell to allow light to pass through.

The vapor cell could be constructed as follows. From a commercial vendor, one can obtain a number of cells with the dimension of 2 mm diameter X 5 mm height, with windows affixed to the two ends, and a small, open tube protruding from the side. This tube would be connected to a vacuum manifold, through which gaseous Rb would be injected into the cell. A bifiliarly wound heating wire would be used to heat the cell to the planned operating temperature of 90$^{o}$C. A combination of Argon and Nitrogen gas would be loaded into the cell, and a CPT resonance would first be observed in a table-top setting. The absolute pressures of each species of gas, and the ratios thereof, would be optimized. Once the pressures are set, a torch would be used to seal the protruding tube. The resulting cell would then be mounted in the assembly shown in figure 20. The overall system is shown in fig. 17 with only one of the two possible physics packages. The overall dimension of this system is 5 cm X 4.5 cm X 1.4 cm, for a total volume of 31.5 $cm^3$. Both configurations of physics packages can be accommodated in these volumes.

The clock could be operated as follows. The OCXO would be locked to a frequency synthesizer with a 10 MHz output, using a phase locked loop. For initial test, one can use a conventional synthesizer. However, as discussed next in the power budget analysis, the final device would require an ASIC-based synthesizer in order to meet the power requirement. The output of the OCXO would drive the DFB laser at 3.4 GHz. The particular OCXO that can be used is the CTS Electronic Components VFOV405. Its 1-second Allan deviation is ~$1X10^{-11}$. The micro-controller, which would have several A/D converters and D/A converters, would control the overall operation of the clock. A modulation signal would be applied to the laser current to produce the error signal for locking one of the sidebands to a resonance. Another modulation would be applied to the phase locked loop, and the corresponding demodulated signal would be used to stabilize the clock, by providing a feedback to the OCXO.

**Table 2: Power Estimate for the Rb-CPT clock**

| | Power (mW) | |
|---|---|---|
| **Component** | **Rb-CPT** | **CSAC** |
| Control and Detection | 41 | 41 |
| 10 MHz Oscillator | 120 | 7 |
| Microwave Synthesis | 25 | 53 |
| DC Laser Power | 6 | 3 |
| Magnetic Field | 4 | 1 |
| Temperature Management | 39 | 7 |
| Power Conditioning | 15 | 13 |
| **Total** | **250** | **125** |

**Power Consumption Estimation:** The total power consumption estimate for the miniature Rb-CPT clock system is given in Table 2, along with the actual power consumption for the prototype CSAC for comparison. Control and detection could be accomplished in the same manner as was done in the CSAC, using a commercial microcontroller, such as the Texas Instruments MSP430, and external programmable high-bit-depth ADCs. As the architecture of this system is very similar to that used in the CSAC, the same power consumption of 41 mW is estimated for it. For the 10 MHz oscillator, a compact, low-power commercial unit, such as the CTS VFOV405, could be used. This particular oscillator draws 120 mW of power during operation, so that amount has been allocated in the power consumption estimate.

The microwave synthesizer necessary to generate the 3.4 GHz modulation tone for the laser could be generated using a custom ASIC. Such ASICs have been developed at 4.6 GHz for use with cesium atomic clocks and demonstrated in their operation. These published ASICs draw less than 15 mW of power. This low power draw is the key reason to use an ASIC in such as clock. The CSAC uses commercially-available PLL chips to generate the required microwave tone. While this is effective, the resulting system draws 53 mW of power. Given the large power draw of the OCXO required for good short-term stability of the output, and given the substantial power demands of the heating system (see below), the use of 53 mW of electrical power to run the frequency synthesizer would make it total power consumption rather high. Thus, an ASIC would have to be developed for this design. Allowing a margin for a higher RF drive power for the higher-power laser to be used in this system, 25 mW is allotted for the microwave synthesis

power consumption. The DC laser power has been estimated to be 6 mW, corresponding to a laser with >1 mW of optical power. This is more than sufficient for the proposed clock design, and the actual power used may be lower. The magnetic field power consumption would be higher than that used by the CSAC, due to the larger cell size.

There are two optical components that would require critical temperature management: The DFB laser and the rubidium cell. To minimize the need for cooling, the operating temperatures for the cell would be set to ~90°C, consistent with the maximum environmental temperature (85°C) generally encountered in practical applications. The heating power necessary to maintain the rubidium cell at 90°C can be calculated using the simple heat transfer model that was used for the CSAC cell. The cell to be used is 2 mm by 2 mm in cross-section and 5 mm long. Assume that the cell has the same emissivity as the CSAC cell ($\varepsilon = 0.57$) and that the evacuated enclosure system has (due to the larger components) a thermal conduction resistance of 500°C/mW. Then, in the worst-case scenario of the cell radiating directly into the lowest expected environmental temperature of -40°C, the power draw necessary to maintain the cell at temperature is ~19 mW.

The laser temperature would be controlled by a TEC. TECs operate most efficiently when the temperature of their "hot" side (the side with the heat sink) is very near the temperature of the "cold" side (the side with the laser). At the lowest ambient temperatures required for the design being considered here, the heat sink would be very efficient at heat removal and the temperature gradient would be small, while at higher ambient temperatures, the efficiency of the TEC would be worse. Since the laser would be designed to be operated at 90°C, the environmental temperature would always be lower than the laser temperature and the TEC will always operate efficiently. Based on the performance curves for a commercially-available miniature TEC (Custom Thermoelectric 00301-9X30-10RU2), at low ambient temperatures, the TEC would require ~0.1 A at ~0.04 V, or 4 mW of electrical power, to remove the ~10 mW of heat generated by the laser. At 85°C ambient, no more than 0.28 A at 0.12 V, or 33.6 mW of electrical power, should be required to remove the heat. Thus, the total power necessary for thermal management of the cell and the DFB laser should range from 29 mW to 36 mW. Specifically, 39 mW has been allotted for this part in the power estimation. Finally, the CSAC uses 13 mW for power conditioning; 15 mW has been allotted for our design. This results in a total power estimate for the miniature Rb-CPT clock of 250 mW.

## 4. Technical Summary (Year 4 – No-cost extension)

### A. Development of Repeated Query Technique for Ramsey Clock

We have demonstrated a new repeated query technique (RQT) with the Ramsey scheme. We discuss its advantages in enhancing the central fringe amplitude and suppressing the side fringes, thus, alleviating the problems associated with the conventional two-pulse Ramsey scheme or single query technique (SQT). We have shown that RQT is suitable for producing narrow linewidth central fringe as a single resonance with high $S/N$ ratio. Since RQT requires only electronic modification of the pulse sequence, it can be implemented without adding complexity to miniaturization of the Ramsey clock. We have conducted detailed experimental and theoretical investigations of RQT by comparing its performances side by side with SQT. We have performed experiments using a 2 cm long rubidium cell and provided theoretical understandings of our results using two physical models for RQT: the Fourier analysis and the

density-matrix model. The theoretical models confirm the expected $S/N$ improvement with $N$, where $N$ represents the number of query pulses in RQT. We have measured frequency stability of a Ramsey clock laboratory prototype by employing SQT and RQT.

## A1. Experimental Description

Fig. 21 shows the schematic diagram of our experimental system developed for investigating the new Ramsey scheme. The experimental system incorporates all necessary servo controls needed to implement the Ramsey clock and measure its frequency stability performance. A frequency-modulated laser beam is produced by sending light from a tunable single-frequency diode laser ($\lambda$ = 795 nm) through a fiber-coupled electro-optic modulator (EOM, bias $V_\pi = 1.4$ V). The EOM is driven by RF signal with frequency equal to half the hyperfine ground-state frequency

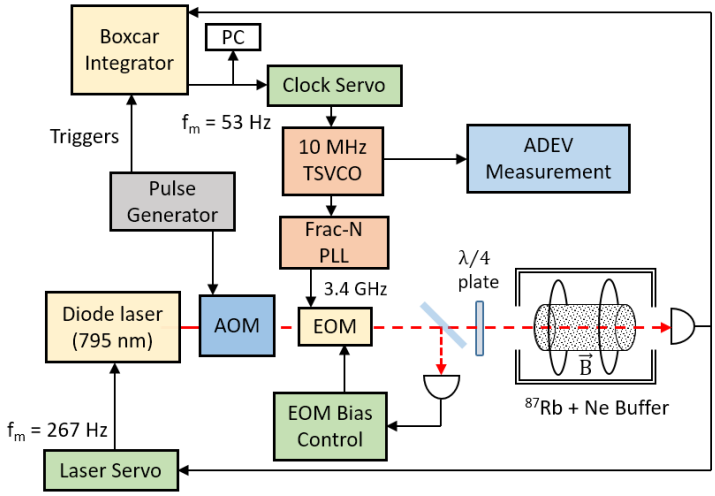


Fig. 21 Schematic of the experimental setup used to generate Ramsey interference in the rubidium atomic clock. The optical beam is pulsed using an AOM and a boxcar integrator is used to perform gated detection and sample averaging to produce the Ramsey fringes by repeated query pulses.

(i.e. 3.417 GHz) in $^{87}$Rb atoms. This creates optical sidebands with a frequency difference of 6.834 GHz. These optical sidebands are used in Raman excitation and producing CPT phenomenon in the rubidium cell (2 cm long). The EOM bias voltage is actively controlled to minimize optical power in the carrier. This is done by measuring a small fraction of the beam after the EOM with the photodiode and controlling the EOM bias voltage by an electronic servo. The RF signal driving the EOM is synthesized from a 10 MHz temperature-stabilized voltage controlled oscillator (TSVCO) by a fractional phase-locked loop (PLL) shown in the figure. The experimental system is operated as a clock by locking the 10 MHz output frequency from the TSVCO to the peak of the central Ramsey fringe by engaging the clock servo. The frequency stability of the locked TSVCO is measured by the Allan deviation (ADEV) measuring instrument.

During experiment, the laser frequency is locked to the absorption maximum in $^{87}$Rb D1 line corresponding to resonant excitation with $|F' = 2\rangle$ excited state . As shown in fig. 21, the output from a single photodetector has been used to implement both the laser servo and the clock servo.

The laser beam is dithered (or frequency modulated) via EOM at two different frequencies ($f_m$ = 267 Hz and 53 Hz, respectively) for the laser servo and the clock servo to operate independently. The servo consisted of lock-in-amplifier and proportional-integral (PI) controller which generate the control signal by demodulating and integrating the photodetector output at the dither frequency. A free-space acousto-optical modulator (AOM, $f_c$ = 80 MHz) is used as a switching

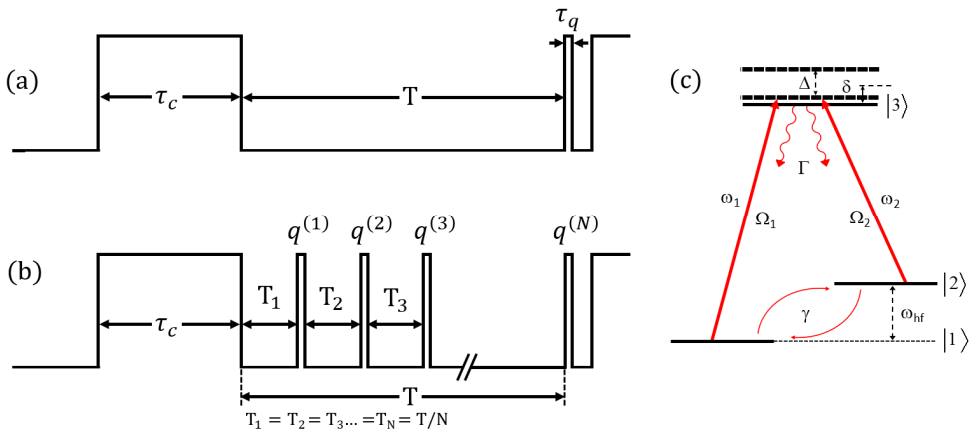


Fig. 21 Timing diagram showing the pulse cycle with (a) a single query pulse, and (b) repeated query pulses for generating Ramsey interference. The pulse cycle in (b) consists of a periodic train of $\boldsymbol{N}$ query pulses $\boldsymbol{q^{(N)}}$ of duration $\boldsymbol{\tau_q}$ each and separation $T_N$ = T/N. A three-level (Λ-type) atomic system shown in (c) has been used to simulate the Ramsey interference phenomena.

element for generating the Ramsey pulse sequence shown in figures 22 (a,b). In case of SQT, the pulse cycle (shown in fig. 22a) is defined by the CPT pulse (duration $\tau_c$), free-evolution time T, and a single query pulse of duration $\tau_q$. For our experiments, $\tau_c$ is chosen to be 500 μs to prepare the atoms in the 'dark state'. The free-evolution time T is chosen to be 1.5 ms which is decided on the basis of dephasing time of the 'dark state' in the medium. The duration of the query pulse $\tau_q$ is chosen to be short (i.e. 1 $\mu$s) to minimize the destructive read-out effect. Fig. 22b shows the modified pulse cycle for RQT using $N$ repeated query pulses. In this case, the free evolution time $T$ in SQT is divided into $N$ equal time periods (i.e. $T_1 = T_2 \ldots = T_N = T/N$) as shown in fig. 22b. Therefore, a single pulse cycle of RQT consists of one CPT pulse of duration $\tau_c$ followed by a periodic train of $N$ free-evolution times $(T_1, T_2 \ldots T_N)$ and $N$ query pulses $\left(q^{(1)}, q^{(2)} \ldots q^{(N)}\right)$ each with duration $\tau_q$.

The pulse generator driving the AOM is programmed to switch the AOM on and off at appropriate time intervals to implement SQT or RQT. The pulsed optical beam is passed through a quarter-wave ($\lambda/4$) plate to create circularly polarized CPT fields. It is then passed through a pure-isotope $^{87}$Rb vapor cell (length = 2 cm, diameter = 1 cm) filled with 10 Torr neon buffer gas. The physics package of the vapor cell consists of a dual layer μ-metal magnetic shield enclosure and a pair of Helmholtz coils mounted inside the enclosure to apply a small uniform axial magnetic field (B ≃ 30 mG) which lifts the Zeeman degeneracy of the $^{87}$Rb energy levels. The vapor cell is also actively temperature controlled ($\Delta T$ ≃ 100 mK). A boxcar integrator is used to gate and integrate the photodetector output during the query pulse for observing Ramsey interference. In case of RQT, the boxcar is triggered by multiple query pulse triggers, and Ramsey interference due to $N$ query pulses is produced by choosing the number of sample

average in the boxcar equal to N. Alternatively, instead of boxcar, we have used a computer interfaced digitizer board to acquire Ramsey fringes. This method gives the advantage of introducing real-time signal processing in data acquisition for reducing 'noise' in Ramsey signal. Ramsey fringes are generated by repeating the pulse cycles in SQT and RQT and slowly changing the frequency difference between the laser fields around the two-photon resonant frequency (i.e. $^{87}$Rb ground-state hyperfine frequency, 6.834 GHz).

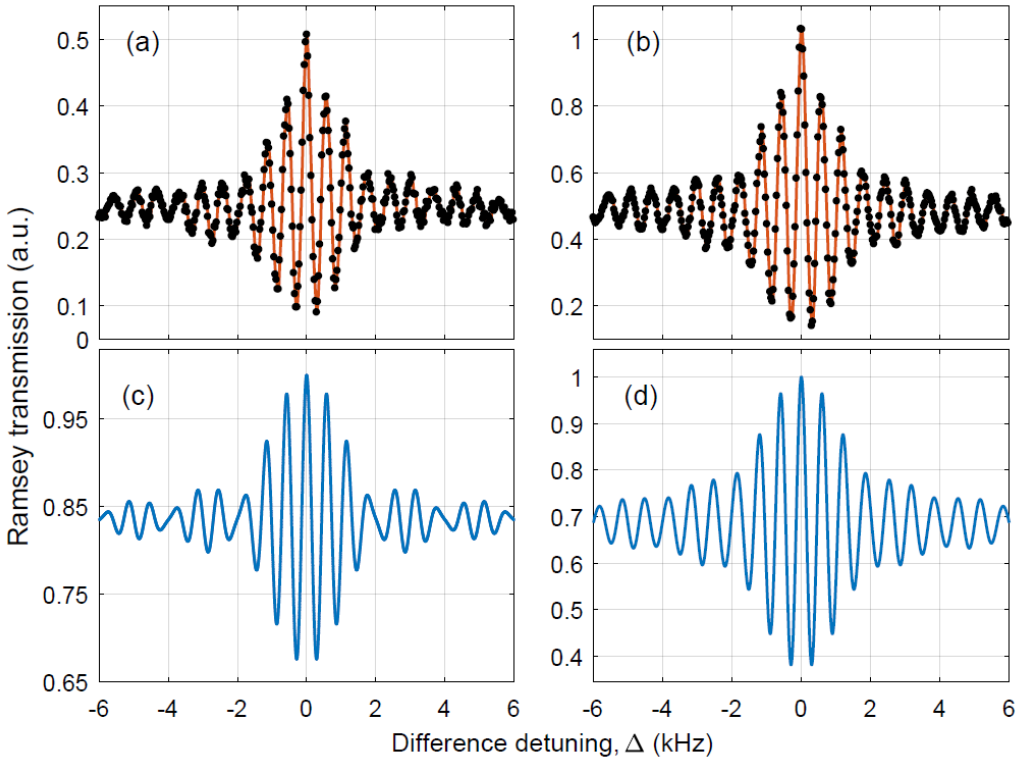


Fig. 23 Experimentally generated Ramsey fringes by using SQT ($\boldsymbol{N}$=1) and total optical power of (a) 57 μW and (b) 90 μW in the CPT beams. Simulated Ramsey fringes for $\boldsymbol{\Omega}$ equals to (c) $\boldsymbol{\Gamma/200}$, and (d) $\boldsymbol{\Gamma/100}$. The following simulation parameters were also used: $\boldsymbol{\tau_c = 500\,\mu s}$, $\boldsymbol{T = 1.5\,ms, \tau_q = 1\,\mu s, \Gamma = 6\,MHz}$, and $\boldsymbol{\gamma_1 = \gamma_2 = \gamma = 60\,Hz}$.

## A2. Results and Discussions

Figures 23(a,b) show measured SQT based Ramsey fringes, obtained by increasing the average optical power in the CPT pulses from 57 $\mu$W to 90 $\mu$W. We used a pulse cycle with $\tau_c$= 500 $\mu$s, $T$ = 1.5 $m$s and $\tau_q$= 1 $\mu$s. Ramsey fringes were generated by scanning the two-photon difference detuning, $\Delta = \left[(\omega_1 - \omega_2) - \omega_{hf}\right]$ slowly at a rate 20 mHz around $\Delta = 0$, where $\omega_1$ and $\omega_2$ correspond to laser frequencies involved with the Raman excitation in a three level $\Lambda-$system shown in fig. 22c. The measured fringe-width is found to be consistent with $\Delta\nu(= 1/2T) \simeq$ 333 Hz and independent of the optical power. The central Ramsey fringe in fig. 23a exhibits a contrast $C(= T_A/T_P)$ of nearly 80% where $T_A$ is the transmitted amplitude and $T_P$ is the peak amplitude of the fringe. Fig. 23b shows central Ramsey fringe with even higher contrast ($C \simeq$ 90%) due to increased (i.e. approximately double) optical power. However, Ramsey fringes adjacent to the center are also found to have high contrast (i.e. close to 76%) in fig. 23b. This

makes the central fringe less distinguishable from being used as a reference signal in the atomic clock. We have closely investigated this aspect of Ramsey fringes theoretically by modeling the Raman excitation in a three-level $\Lambda-$system shown in fig. 22c with the density-matrix equations: $i\hbar\frac{\partial\rho}{\partial t}=[H\rho-\rho H^{\dagger}]+L$ where $\rho$ is the density operator, H is the semi-classical, non-Hermitian Hamiltonian, and $L$ represents the source matrix accounting for possible relaxations (i.e. Γ and $\gamma$) between the atomic states [10]. Under the rotating wave approximation, and in the rotating wave picture, the Hamiltonian $H$ and the source matrix $L$ for this three-level atomic system are described by

$$H=\begin{pmatrix}\frac{\Delta}{2}-\frac{i\gamma}{2} & 0 & -\frac{\Omega_1}{2}\\ 0 & -\frac{\Delta}{2}-\frac{i\gamma}{2} & -\frac{\Omega_2}{2}\\ -\frac{\Omega_1}{2} & -\frac{\Omega_2}{2} & -\delta-\frac{i\Gamma}{2}\end{pmatrix},\qquad L=\begin{pmatrix}\frac{\Gamma}{2}\rho_{33}+\frac{\gamma}{2}\rho_{22} & 0 & 0\\ 0 & \frac{\Gamma}{2}\rho_{33}+\frac{\gamma}{2}\rho_{11} & 0\\ 0 & 0 & 0\end{pmatrix} \tag{3}$$

where $\Omega_1$and $\Omega_2$ correspond to the Rabi frequencies of the CPT fields, $\delta=(\delta_1+\delta_2)/2$ is the average (or common-mode) frequency detuning with $\delta_1$ and $\delta_2$ representing the single-photon detunings of the respective CPT fields, and $\Delta=\delta_1-\delta_2$ corresponds to two-photon difference detuning between the CPT fields. For simplicity in modeling, $\Omega_1$and $\Omega_2$ are chosen to be equal i.e. $\Omega_1=\Omega_2=\Omega$.

The density-matrix equations established using $H$ and $L$ matrices in eqn. (1) are used to calculate Ramsey fringes produced by the pulsed CPT excitation by choosing $\begin{cases}\Omega\neq 0,\ t=\tau_c,\tau_q\\ \Omega=0,\ t=T\end{cases}$. For SQT pulse cycle, numerical solutions for $\rho$ at the end of three sequential time evolutions $\tau_c$, $T$, and $\tau_q$ are obtained using different values of $\Delta$ around $\Delta=0$. We picked the density-matrix element $\rho_{33}$ corresponding to excited-state population for plotting Ramsey fringes. The model is also extended to find numerical solutions for $\rho$ with RQT by including $N$ equal free-evolution times (i.e. $T_1=T_2\ldots=T_N=T/N$) and $N$ query pulses (i.e. $q^{(1)},q^{(2)}\ldots q^{(N)}$) of equal duration $\tau_q$ in the pulse cycle. In this case, Ramsey fringes are calculated by successively adding the values of $\rho$ after each query pulse $q^{(i)},i=1..N$. Figures 23(c,d) show calculated SQT based Ramsey fringes using the simulation parameters: $\tau_c$ = 500 μs, T = 1.5 ms, $\tau_q$ = 1 μs, and $\Gamma$ = 6 MHz which is similar to the decay rate of rubidium. These figures are compared with the experimental results in figs. 23(a,b) and are obtained by changing the Rabi frequency, Ω from $\Gamma/200$ to $\Gamma/100$ (equivalent to doubling of optical power in the experiment) and by introducing an empirical ground-state decoherence rate $\gamma$ = 60 Hz. Calculated fringes in figs. 3(c,d) show a noticeable change in the fringe envelope due to increase in the Raman saturation parameter ($\Omega\,\tau_c$) of the CPT pulse. The condition $\Omega\,\tau_c\gg 1$ leads to a near steady-state Raman excitation condition [10]. Fig. 23c shows the pulse-transform limited fringe envelope for $\Omega=\Gamma/200$ which can be described by the function $sinc(\Delta\tau_C/2)$. This also shows similarity with the experimental fringe envelope in fig. 23a. The central Ramsey fringe in fig. 23c has a contrast of nearly 32.4%. Fig. 23d shows the fringe envelope for $\Omega=\Gamma/100$ which resembles the steady-state CPT line shape with no sidelobes. The central fringe contrast is found to be ≃ 61.8% which higher than the previous case. It is also important to note that the results obtained from our

theoretical model cannot be used to exactly match the experimental results. However, the model shows general characteristics of Ramsey interference formed by SQT.

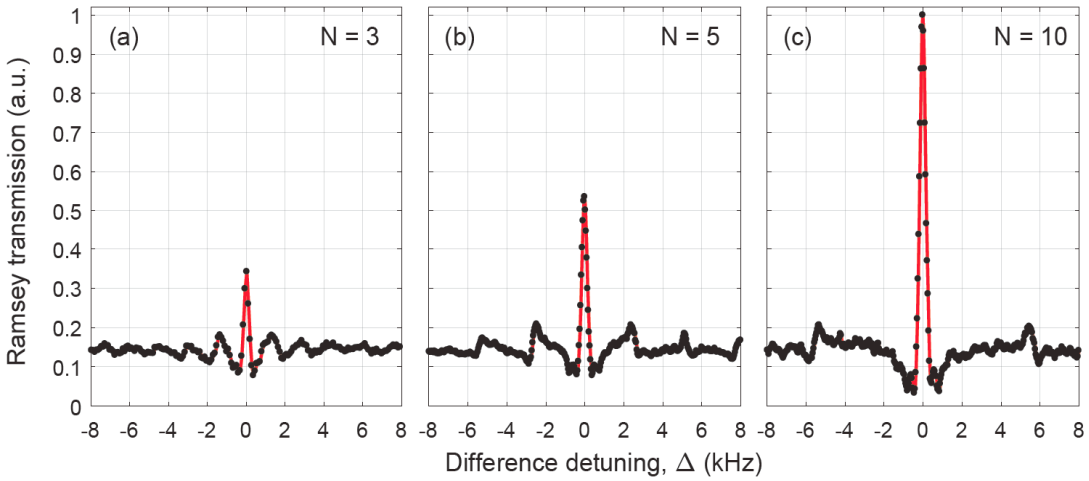


Fig. 24 Experimental Ramsey fringes collected via RQT with (a) $\boldsymbol{N}$=3 (b) $\boldsymbol{N}$=5, and (c) $\boldsymbol{N}$=10 query pulses. The background biases were electronically subtracted and kept equal when measuring the signal contrast.

Figs. 24(a-c) show experimentally measured Ramsey fringes by using $N$ = 3, 5, and 10 query pulses in the RQT pulse cycle and 57 $\mu$W average optical power in the CPT pulses. In all these cases, the central fringe distinctly emerges as a single resonance in the Ramsey spectrum. The side fringes are suppressed due to combined interference of N query pulses, and the peak amplitude of the central fringe is increased in proportion with $N$ which is desirable since the

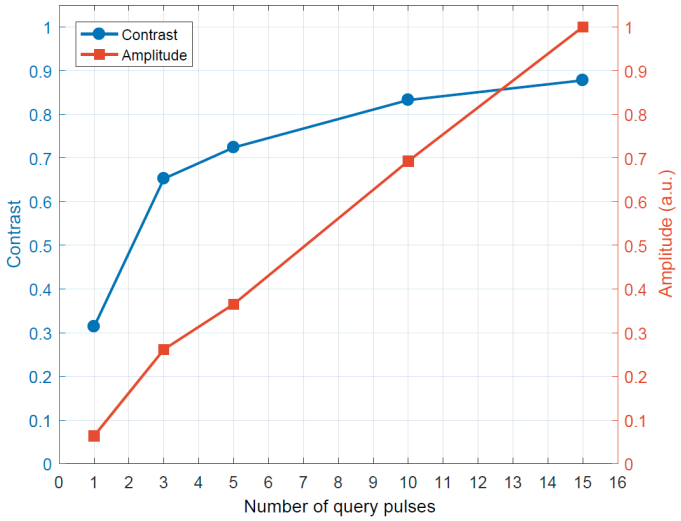


Fig. 25 Variation in fringe contrast and amplitude with query pulses, measured experimentally.

central fringe is used in creating the clock discriminant signal. We measured the contrast in the Ramsey signal by defining it as $(T_p - T_b)/T_p$ where $T_b$ is the background transmission. The contrasts are found to be approximately 65%, 72%, and 83% for N = 3, 5, and 10 query pulses, respectively. Fig. 25 shows the variation in contrast and peak (or signal) amplitude as a function

of $N$. While the signal amplitude continues to grow linearly, the contrast reaches a maximum value 87% at around $N$ = 15. The result suggests that RQT can produce a discriminant signal with significantly high contrast and $S/N$ ratio, as needed to achieve high short-term frequency stability in the atomic clock. It is also observed that increase in the peak amplitude is accompanied by a small increase in the fringe-width and substantial increase in the overall bias with $N$. As the bias is created by the electronic addition of query pulse signals, we compensated it electronically.

We simulated the Ramsey fringes produced due to RQT using our atomic model. Fig. 26a-c shows the simulated Ramsey spectra using repeated query pulses with N = 3, 5, and 10, respectively. All other simulation parameters are kept the same as SQT except the free-evolution time between the query pulses are chosen to be $T_1 = T_2 \ldots = T/N$ with $T$ = 1.5 ms. Theoretical Ramsey spectra obtained with RQT for $\Omega = \Gamma/200$ show striking similarity with our experimental results in fig. 24. Due to constructive interference of all query pulses at the fringe center $\Delta = 0$, a single-peaked Ramsey fringe with narrow fringe-width ($\Delta\nu$ comparable to $1/2T$

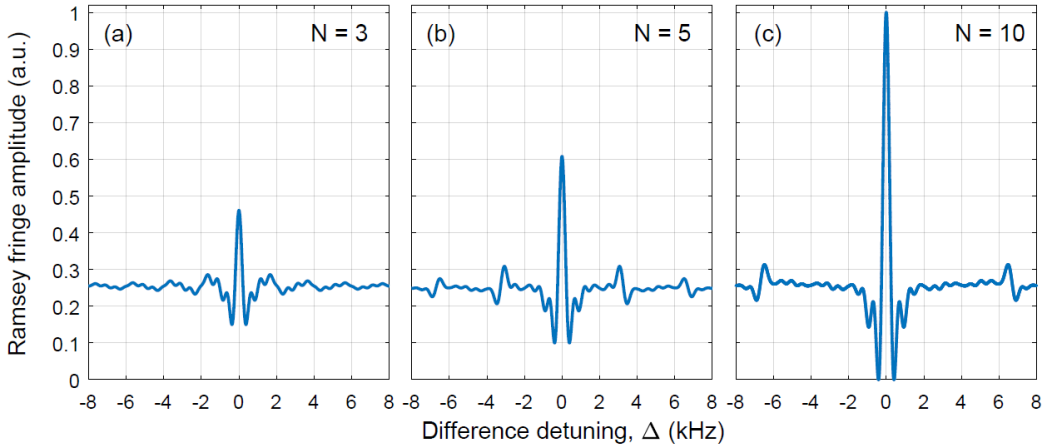


Fig. 26 Simulated Ramsey fringes with (a) $\boldsymbol{N}$=3 (b) $\boldsymbol{N}$=5, and (c) $\boldsymbol{N}$=10 query pulses. The following simulation parameters were used: $\boldsymbol{\tau_c}$ = 500 µs, T = 1.5 ms, $\boldsymbol{\tau_q}$ = 1 µs and $\boldsymbol{\Omega = \Gamma/200}$.

$=$ 333 Hz) is produced. Increasing bias resulting from addition of repeated query signals, has been suppressed while plotting the Ramsey spectra in fig. 26. As in experiment, the fringe amplitude enhancement has been confirmed from the simulation which, in practice, leads to improvement in contrast and $S/N$ ratio in RQT.

A general understanding about fringe amplitude enhancement due to RQT can be developed by finding the following analytical expression as the weighted sum of periodic Ramsey signals from N query pulses as

$$R(\Delta) = \sum_{n=1}^{\mathrm{N}} \cos\left(n\,\frac{\Delta.\mathrm{T}}{N}\right) e^{-n\gamma\frac{\mathrm{T}}{N}}$$

$$= \frac{e^{-\gamma\,\mathrm{T}}\left\{\cos\left[(\mathrm{N}+1)\,\frac{\Delta.\mathrm{T}}{N}\right] - e^{-\gamma\frac{T}{N}}\cos(\Delta.\mathrm{T})\right\} - \cos\left(\frac{\Delta.\mathrm{T}}{N}\right) + e^{-\gamma\,\frac{T}{N}}}{2\left[\cos\left(\frac{\Delta.\mathrm{T}}{N}\right) - \cosh\left(\gamma\,\frac{\mathrm{T}}{N}\right)\right]} \qquad (4)$$

where $R(\Delta)$ represents the amplitude of Ramsey interference, the fringe line shapes are assumed to be uniform, and the fringe amplitudes are assumed to decay at the rate $\gamma$. For $\gamma = 0$, the expression reduced to the familiar fringe shape function $\frac{\sin[(N+1/2)\,\Delta\,T/N]}{2\sin[\Delta\,T/2N]}$ which has a maximum value $N$ at $\Delta = 0$ indicating that the signal amplitude will be $N$ times larger. Due to non-zero $\gamma$, the enhancement factor is found from eqn. (2) to be $\frac{e^{\gamma T}-1}{e^{\gamma T/N}-1}$ for N queries. This analytical model does not consider the destructive read-out effect of the query pulses on the fringe amplitude enhancement. Fig. 27 shows the plots of enhancement factors estimated from eqn. (2) and our simulation for comparison purpose. Both simulation and the analytical model show higher slopes for the enhancement factor compared to the case $\gamma = 0$. The solid dots in fig. 27 show our experimental measurements with slope which agrees closely with the analytical model and the simulation for small $N$. The observed discrepancy in the slope may be due to the choice of simulation parameters, particularly $\gamma$ and $\Omega$ not matching the experiment. Degradation in the enhancement factor due to the destructive read-out effect of the query pulses is found to be significant for large $N$ exceeding 30 pulses or so.

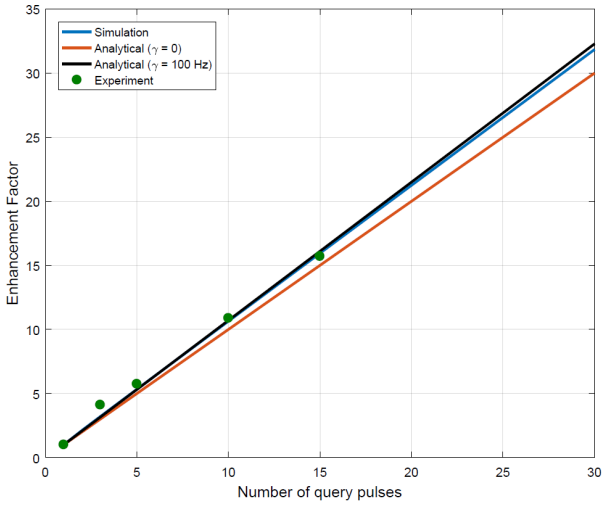


Fig. 27 Amplitude enhancement factor for the Ramsey fringes acquired using $N$ query pulses.

## A3. Ramsey Clock Result

We measured the frequency stability of the clock prototype to compare the performance of RQT with SQT in the Ramsey atomic clock. The boxcar integrator was used to acquire the Ramsey fringes. The frequency of the TSVCO was locked to the center of Ramsey fringe using the clock servo shown earlier in fig. 21. The frequency stability (or ADEV, $\sigma_y$) of the locked TSVCO was measured with the ADEV measurement test probe by referencing it to a rubidium frequency standard. Fig. 28 shows ADEV, $\sigma_y$ as a function of the averaging (or integration) time $\tau$ for $N$ = 1 and 10 query pulses. Under the same condition, RQT with $N$=10 provided better short term stability ($\sigma_y \simeq 5.6\times 10^{-11}$ at $\tau$ = 1 sec) compared to the SQT ($N$ = 1) case. The short-term stability of the clock can be estimated by

$$\sigma_y(\tau) = \frac{1}{Q \cdot SNR}\sqrt{\frac{T_c}{N\,\tau_q}}\;\tau^{-\frac{1}{2}} \qquad (5)$$

where Q = $\omega_{hf}/\Delta\omega$ represents the quality factor of the central Ramsey fringe, $\Delta\omega$ corresponds to the central fringe-width, and $\omega_{hf}$ representing the rubidium hyperfine frequency. Due to pulsed operation of the Ramsey clock, $\sigma_y$ in eqn. (3) includes a factor in the square root as the ratio of pulse cycle time $T_c\left(= \tau_c + T + \tau_q\right)$ to the detection time $N\tau_q$. Thus, in the case of RQT, besides improvement in SNR, one can expect an additional improvement in $\sigma_y$ by a factor $\sqrt{N}$. Contrary

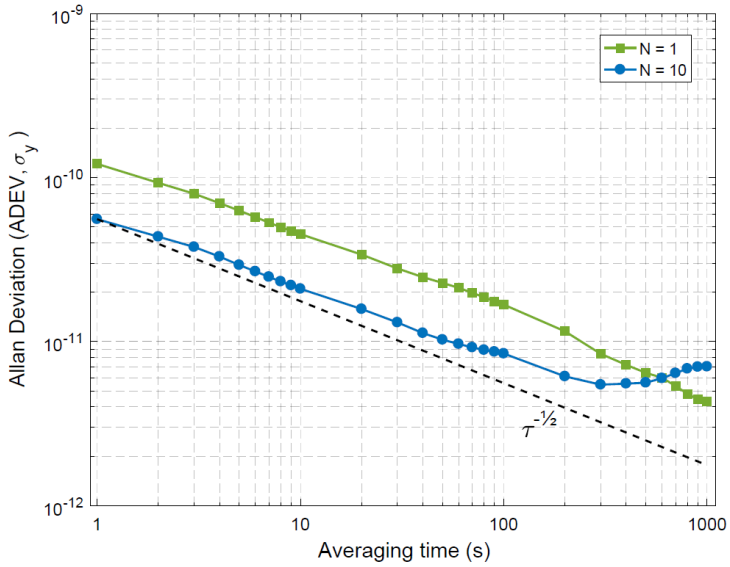


Fig. 28 Frequency stability performance of the rubidium atomic clock measured using ADEV for SQT (green squares) and RQT with N=10 (blue circles). The dashed line represents $\boldsymbol{\sigma_y(\tau)} = 5.58 \times 10^{-11}\ \boldsymbol{\tau^{-1/2}}$.

to these expected improvements, we observed much less improvement (nearly by a factor 2) in the frequency stability, possibly due to various sources of noise in our experiments. However, improved frequency stability with RQT was observed in $\sigma_y$ for $\tau$ ranging up to nearly 100 seconds (fig. 28). Our experimental system has significant noise and drift arising from the cell temperature control and the residual magnetic field. These can be reduced in the future with a better design of the cell physics package to conclusively verify the performance of RQT in the Ramsey clock. Incorporation of the VCSEL to replace the bulky and temperature sensitive EOM and the laser in our system, and improving the design for the cell physics package will minimize the system noise and drift, for improving the long-term stability of the rubidium clock.

## B. VCSEL characterization

For compactness and low power consumption, the tunable laser and EOM should be replaced by a vertical cavity surface emitting laser (VCSEL), which can be directly modulated at RF frequencies. We have begun preliminary studies with a VCSEL (M2 Photonics VCSEL, APM2101013300) to characterize its modulation behavior and performance for generating CPT and RR interference fringes. The VCSEL is current-driven and temperature controlled with an ILX laser controller with a 5 mA/V current tuning slope and a measured wavelength and frequency tuning of $\lambda/I$ = 0.6646 nm/mA or 103 GHz/mA. Because of this sensitivity, a very low noise current driver is required. The size of a VCSEL diode (fig. 29) makes it an ideal option for size and power requirements in compact clocks. The VSCEL linewidth, however, is around 30

MHz, which is significantly higher than a tabletop tunable diode laser (~1 MHz) and will reduce the performance of the clock.

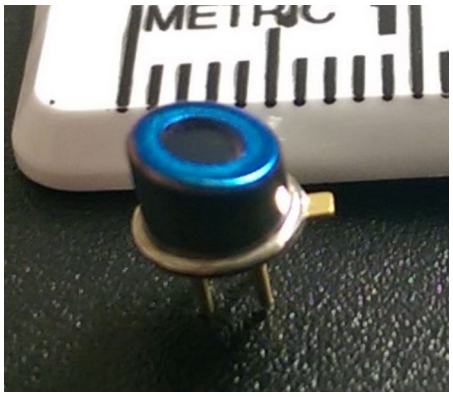

Fig. 29 VCSEL in a TO-86 package, less than half a cm in diameter

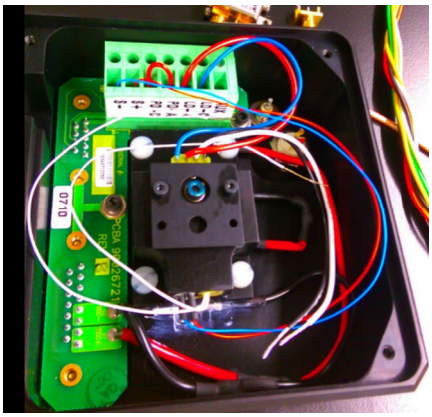

Fig. 30 VCSEL ILX mount with TEC and thermistor, the VCSEL is connected to the current source.

The VCSEL frequency is tuned by both current and temperature, therefore precise temperature control is also implemented. Fig. 30 shows the TEC heating block and diode mount used in the setup. For VCSEL sideband modulation, a bias-tee is used to combine the DC current from the low-noise current driver and the RF signal at 3.417 GHz from a VCO.

Preliminary measurements of modulated VCSEL with the Fabry-Perot scanning etalon showed a high sensitivity to RF amplitude. However, at an RF power of 10 dBm, the carrier is sufficiently suppressed and optical sidebands separated by 6.834 GHz were visible, though noisy. Further study is needed for sideband generation and application of VCSEL to our schemes

## 5. Activities and Recognition

### Year-1

1. PI visited NU in July, 2013 to discuss about project collaboration.

2. The PI attended SPIE Photonics West meeting, Feb. 2014 in San Francisco and served on the Program Committee for the session on '*Advances in Slow and Fast Light – VII*'. The PI also gave the invited talk titled 'Investigations of AC Stark shift in pulsed Raman-Ramsey interaction for vapor cell clock development' at the conference.

### Year-2

1. The PI served as a member of the 'Program Committee' in the session on '*Slow Light, Fast Light and Opto-Atomic Metrology-VIII*' organized by SPIE Photonics West Meeting in Feb. 2015, San Francisco, CA. The PI gave an invited talk titled 'AC Stark shift in Raman-Ramsey interference using a multi-level system calculation' at the conference.

2. Graduate student, Mr. Zachary Warren presented a paper titled "Measurements and characterization of a Rb-based Raman-Ramsey vapor cell atomic clock" in the session on '*Slow Light, Fast Light and Opto-Atomic Metrology-VIII*' organized by SPIE Photonics West Meeting in Feb. 2015, San Francisco, CA.

3. Co-I, Dr. Renu Tripathi served as a member of the SPIE Society Scholarship Committee.

4. Co-I, Dr. Renu Tripathi received the DURIP award from Army Research Office (ARO) for the development of a long range, high resolution laser detection and ranging (LADAR) system.

   *Project Title:* Instrument Development for a Long-Range, High-Resolution 3D Imaging Photon Counting LADAR
   PI: Renu Tripathi
   Funding Agency: DOD DURIP
   Award Amount: $191,079.80
   Duration: July 15, 2015-Jan 15, 2017.

**Year-3**

1. PI served as a member of the 'Program Committee' in the session on '*Slow Light, Fast Light and Opto-Atomic Metrology-X*' organized by SPIE Photonics West Annual Meeting in Feb. 2016, San Francisco, CA.

2. The PI served as the '*Lead of the Organizing Committee'* in organizing the *Delaware Optics Symposium* on October 8-9, 2015 at DSU campus. The PI invited several renowned researchers to the DSU campus to deliver invited talks on emerging topics in Optics and Photonics during this symposium, and helped in organizing technical sessions, poster sessions, and an industry exhibit.

3. The Co-I, Dr. Renu Tripathi served as a member of the SPIE Society Scholarship Committee.

4. Awarded the *O*STAR Center* – Optics for Space Technology & Applied Research Center at DSU under the NASA MIRO 2015 program (center award, Award No. NNH14ZHA001N-MIRO, Period Covered: 09-15 - 08-20). The Co-I, Dr. Renu Tripathi is leading a subproject in O*STAR Center on the Development of sodium LADAR.

**Year-4 (No-cost extension)**

1. Graduate student, Mr. Zachary Warren defended the Ph.D. thesis titled 'Coherent Population Trapping and Optical Ramsey Interference for Compact Rubidium Clock Development' on Dec. 6, 2016.

2. Graduate student, Mr. Zachary Warren presented a paper titled 'Two-photon Resonant Ramsey Interference using a Repeated-Query Scheme for Atomic Clock Development'

in *APS Mid-Atlantic Meeting 2016* organized at University of Delaware campus on Oct.15, 2016.

## 6. Journal Publications

1. M.S. Shahriar, Ye Wang, S. Krishnamurthy, Y. Tu, G.S. Pati and S. Tseng, 'Evolution of an N-level system via automated vectorization of the Liouville equations and application to optically controlled polarization rotation,' J. Mod. Opt. 61, 351 (2014).

2. G.S. Pati, Z. Warren, N. Yu and M.S. Shahriar, "Computational studies of light shift in a Raman-Ramsey interference-based atomic clock," J. Opt. Soc. Am. B 32, 388-394 (2015).

3. Z. Warren, S. Shahriar, R. Tripathi and G.S. Pati, "Experimental and Theoretical Comparison of Different Optical Excitation Schemes for a Compact Coherent Population Trapping Rb Vapor Clock," (Submitted to Metrologia, IOP Science, 2017).

4. Z. Warren, S. Shahriar, R. Tripathi and G.S. Pati, "Repeated Query Ramsey Interference for Enhanced Atomic Clock Stability," (manuscript to be submitted, 2017).

5. M. E. Kim, R. Sarkar, R. Fang, S. M. Shahriar, "N-atom collective-state atomic clock with √N-fold increase in effective frequency & √N-fold reduction in fringe width", Physical Review A 91, 063629 (2015).

6. R. Sarkar, M. E. Kim, R. Fang, Y. Tu, S. M. Shahriar, "Effects of non-idealities & quantization of the center of mass motion on symmetric & asymmetric collective states in a collective state atomic interferometer", Journal of Modern Optics 62, 1253 (2015).

7. R. Sarkar, M. E. Kim, R. Fang, S. M. Shahriar, "N-atom collective-state atomic interferometer with ultrahigh Compton frequency & ultrashort de Broglie wavelength, with √N reduction in fringe width", Physical Review A 92, 063612 (2015).

## 7. Conference Publications

1. Investigations of AC Stark shift in pulsed Raman-Ramsey interaction for vapor cell clock development
   Gour Pati, Z. Warren and S. Shahriar, presented at the SPIE Photonics West, *Advances in Slow and Fast Light VII*, Feb. 5, 2014, San Francisco, CA.

2. Measurements and characterization of a Rb-based Raman-Ramsey vapor cell atomic clock
   Gour Pati, Z. Warren, Renu Tripathi and S. Shahriar, presented at the SPIE Photonics West, *Slow Light, Fast Light and Opto-Atomic Precision Metrology - VIII*, February, 2015, San Francisco, CA.

3. AC Stark shift in Raman-Ramsey interference using a multi-level system calculation

Gour Pati, Z. Warren and S. Shahriar, presented at the SPIE Photonics West, *Slow Light, Fast Light and Opto-Atomic Precision Metrology - VIII*, February, 2015, San Francisco, CA.

4. Two-photon resonant Ramsey interference using a repeated-query scheme for atomic clock development
   Z. Warren, R. Tripathi and G. Pati, presented at *APS Mid-Atlantic Meeting 2016* organized at University of Delaware campus on Oct.15, 2016.